

Review

## III–V semiconductor nanowires for optoelectronic device applications

Hannah J. Joyce<sup>a,\*</sup>, Qiang Gao<sup>a</sup>, H. Hoe Tan<sup>a</sup>, C. Jagadish<sup>a</sup>,  
Yong Kim<sup>b</sup>, Jin Zou<sup>c</sup>, Leigh M. Smith<sup>d</sup>, Howard E. Jackson<sup>d</sup>,  
Jan M. Yarrison-Rice<sup>e</sup>, Patrick Parkinson<sup>f</sup>, Michael B. Johnston<sup>f</sup>

<sup>a</sup>*Department of Electronic Materials Engineering, Research School of Physics and Engineering,  
The Australian National University, Canberra, ACT 0200, Australia*

<sup>b</sup>*Department of Physics, College of Natural Sciences, Dong-A University, Hadan 840, Sahagu,  
Busan 604-714, Republic of Korea*

<sup>c</sup>*School of Engineering and Centre for Microscopy and Microanalysis, The University of Queensland,  
St. Lucia, QLD 4072, Australia*

<sup>d</sup>*Department of Physics, University of Cincinnati, Cincinnati, OH 45211, USA*

<sup>e</sup>*Department of Physics, Miami University, Oxford, OH 45056, USA*

<sup>f</sup>*Clarendon Laboratory, Department of Physics, University of Oxford, Parks Road,  
Oxford OX1 3PU, United Kingdom*

Available online 9 April 2011

---

### Abstract

Semiconductor nanowires have recently emerged as a new class of materials with significant potential to reveal new fundamental physics and to propel new applications in quantum electronic and optoelectronic devices. Semiconductor nanowires show exceptional promise as nanostructured materials for exploring physics in reduced dimensions and in complex geometries, as well as in one-dimensional nanowire devices. They are compatible with existing semiconductor technologies and can be tailored into unique axial and radial heterostructures. In this contribution we review the recent efforts of our international collaboration which have resulted in significant advances in the growth of exceptionally high quality III–V nanowires and nanowire heterostructures, and major developments in understanding the electronic energy landscapes of these nanowires and the dynamics of carriers in these nanowires using photoluminescence, time-resolved photoluminescence and terahertz conductivity spectroscopy.

*Keywords:* Nanowire; III–V semiconductors; Growth; Photoluminescence; Electron microscopy; Terahertz spectroscopy

---

\*Corresponding author. Present address: Clarendon Laboratory, Department of Physics, University of Oxford, Parks Road, Oxford OX1 3PU, United Kingdom.

*E-mail address:* h.joyce1@physics.ox.ac.uk (H.J. Joyce).

**Contents**

1. Introduction . . . . .	24
2. Fabrication of III–V nanowires. . . . .	25
2.1. Template-directed nanowire growth . . . . .	26
2.2. Free-standing nanowire growth . . . . .	27
3. Fundamental principles of III–V nanowire growth by Au-assisted MOCVD . . . . .	28
3.1. Basic growth mechanism . . . . .	28
3.2. Growth procedure. . . . .	29
3.3. Alloying of the Au nanoparticle . . . . .	30
3.4. Axial and radial growth modes . . . . .	31
4. Nanowire morphology and crystal structure. . . . .	32
4.1. Nanowire crystal structure. . . . .	32
4.2. Nanowire side facets . . . . .	33
5. Tailoring nanowire growth . . . . .	35
5.1. Substrate preparation . . . . .	35
5.2. Effects of growth temperature . . . . .	37
5.3. Effects of V/III ratio . . . . .	39
5.4. Effects of growth rate . . . . .	41
5.5. Tailoring multiple growth parameters . . . . .	42
6. Ternary and quaternary nanowires . . . . .	43
7. Heterostructure nanowires . . . . .	45
7.1. Axial nanowire heterostructures . . . . .	45
7.2. Radial nanowire heterostructures . . . . .	47
7.3. Nanowire–substrate heterostructures. . . . .	50
8. Photoluminescence spectroscopy of semiconductor nanowires . . . . .	51
8.1. Photoluminescence emission from nanowires and defects . . . . .	53
8.2. Polarisation spectroscopy of III–V nanowires . . . . .	54
8.3. PL spectroscopic mapping of nanowires . . . . .	57
8.4. Resonant spectroscopy of III–V nanowires . . . . .	59
8.5. Time-resolved photoluminescence spectroscopy . . . . .	60
8.6. Raman characterisation. . . . .	62
8.7. Summary . . . . .	64
9. Terahertz conductivity of semiconductor nanowires . . . . .	64
9.1. Photoconductivity of GaAs nanowires . . . . .	65
9.2. The influence of surface trapping . . . . .	68
9.3. The influence of crystallographic defects . . . . .	70
9.4. Summary . . . . .	71
10. Conclusion . . . . .	71
Acknowledgements . . . . .	72
References . . . . .	72

---

**1. Introduction**

III–V semiconductor nanowires exhibit outstanding potential as nano-building blocks for future devices and systems. These nanowires have been proposed for a wide variety of applications ranging from interconnects to functional device elements in electronic and optoelectronic applications. Nanowire-based sensors, for instance, have remarkable

sensitivity with direct electrical detection of single virus particles and single DNA molecules being reported [1,2]. Nanowire-based optical sensors which use the evanescent field of nanowire waveguides have been demonstrated [3]. Nanowire-based LEDs utilising quantum-dot sections embedded within a nanowire, have demonstrated potential for use as single photon sources operating at room temperature [4–6]. Coaxial nanowire structures acting as solar cells show particular promise [7–9]. III–V nanowires are compatible with existing semiconductor technologies can be readily integrated with Si-based microelectronics, and can be tailored into unique axial and radial heterostructures. In addition to their capacity as one-dimensional nanowire devices, semiconductor nanowires are excellent nanostructured materials for exploring physics in reduced dimensions and in complex geometries.

In imagining new nanowire-based structures with new properties and functionalities, one must keep in mind four central qualities of nanowires: (1) the degree of confinement including possible quantum confinement; (2) the large surface-to-volume ratio intrinsic to nanowires; (3) the length scale defined by the nanowire diameter which has dramatic consequences for the excitation and emission of electronic states in nanowires; and finally (4) the quality of the nanowire growth, the sine qua non, the foundation of every successful nanowire device structure. Successful growth of nanowires involves careful control of quality, alloy composition, diameter, and electronic properties. In this review, we will weave a discussion of the relevance and importance of each of these central qualities in terms of both the basic science and the engineering of device structures.

This contribution focuses on the recent efforts of our international collaboration, towards exceptionally high quality III–V nanowires and nanowire heterostructures for use in quantum electronic and optoelectronic devices. This research has produced significant advances in nanowire growth by metalorganic chemical vapour deposition (MOCVD), and in nanowire characterisation by extensive electron microscopy. We also discuss major advances made using photoluminescence (PL), time-resolved photoluminescence (TRPL) and terahertz conductivity spectroscopy (TCS) towards understanding of the nanowire electronic energy landscapes and the dynamics of carriers in these nanowires.

We begin by providing a general introduction to nanowire growth in Section 2. This discusses why Au-assisted metalorganic chemical vapour deposition (MOCVD) is the technique of choice for III–V nanowire growth. The fundamental principles underlying MOCVD and the Au-assisted growth mechanism are discussed in Section 3. Section 4 describes the morphology and crystallographic structure of the nanowires grown by this technique. In Section 5 we then focus on GaAs nanowires to exemplify how growth parameters can be tuned to give defect-free III–V nanowires with excellent structural and optical properties. Then in Section 6 we turn to the fabrication of ternary nanowires and in Section 7 the fabrication of nanowire heterostructures, which will enable functional nanowire-based electronic and optoelectronic devices. Section 8 discusses the characterisation of the optical and electronic nanowire properties using PL spectroscopy. The electronic properties are described further in Section 9, which discusses terahertz conductivity spectroscopy (TCS) of these nanowires.

## 2. Fabrication of III–V nanowires

The first challenge is to fabricate nanowires with well-controlled dimensions, orientation, structure, phase purity and chemical composition. Nanowire size and shape

are crucial: in the nanoscale regime, even small variations in size can have a large effect on overall device performance. For instance, nanowire dimensions determine the degree of confinement, and consequently affect the behaviour of charge carriers in quantum electronic devices. It is important to control the nanowire diameter, because most device applications require a well-defined uniform diameter. For example, in proposed nanowire lasers, a uniform diameter is critical for a nanowire's performance as a resonant cavity. Phase purity is essential because the crystallographic phase, whether zinc-blende (ZB) or wurtzite (WZ), directly affects the bandstructure and electronic properties of the nanowires. In addition, crystallographic defects such as stacking faults and twin planes create non-radiative recombination centres which adversely affect optoelectronic device performance. Control over chemical composition, for instance to achieve intrinsic and doped nanowires, and nanowire heterostructures, is also essential for emerging nanowire device technologies.

III–V nanowires can be fabricated via a number of approaches. These are classified into two broad categories: top-down and bottom-up. Top-down methods begin with bulk material, from which nanowires are patterned via a combination of lithography and etching, for example using electron beam lithography and plasma etching or focused ion beam milling. Top-down methods have underpinned the microelectronics industry to date, but as the length scales of devices shrink according to Moore's law, top-down methods become increasingly problematic. The lithographic and etching techniques are resolution limited, which makes it difficult to define smaller features, and the quality of the nanostructures diminishes. The etching and patterning processes introduce surface defects, which adversely affect nanostructure properties. Furthermore, the process is intrinsically wasteful and there are large challenges to overcome before these technologies become high-throughput, cost-effective means of nanowire fabrication.

Bottom-up methods, on the other hand, involve the chemical synthesis of nanowires whose properties can be carefully controlled and tuned during growth. These nanowires themselves are building blocks, which can subsequently be assembled into more complex nanoscale devices and architectures. This bottom-up paradigm offers opportunities for the fabrication of atomically precise, complex devices not possible with conventional top-down technologies. Consequently, this paradigm is expected to lead the next generation of nanoscale electronics and optoelectronics. In many ways, bottom-up methods mimic the growth of living organisms, whereby macro-molecules are assembled into larger, more complex structures. A detailed discussion of the wide variety of nanowire fabrication methods is given in the review by Xia et al. [10]. Within the bottom-up fabrication regime, there are two sub-categories of nanowire growth techniques: template directed and free-standing.

### *2.1. Template-directed nanowire growth*

Template-directed methods use a template to confine the crystal growth to a one-dimensional nanowire shape, allowing elongation in only one-dimension while physically restraining growth in other directions. Examples of templates are porous anodised alumina, diblock copolymers, V-grooves and step edges. These templates give reasonable control over the diameter and length of nanowires, are scalable, and produce structures which can be readily integrated with existing devices. The success of these techniques is, however, entirely dependent on the ability to fabricate a suitable template. The quality of

the template directly influences the quality of the grown nanowires. In cases where growth is epitaxial with the template, as with V-groove templates, the template materials limit the types of nanowire material which can be grown epitaxially. Also, the nanowires remain embedded on the substrate which precludes their assembly into complex device architectures. Finally, control of nanowire size is limited by the resolution of the technique used to pattern the template.

## 2.2. Free-standing nanowire growth

The free-standing nanowire growth method relies on anisotropy of growth rates. Generally, nanowires nucleate at a single point and elongate in the growth direction with the highest growth rate. The slower growth rates of other directions constrain the nanowire to a one-dimensional shape. Numerous techniques exist for free-standing nanowire growth, including self-catalysed growth, oxide-assisted growth, vapour–liquid–solid (VLS) growth [11], and solution–liquid–solid growth [12], to name a few. Nanowires can be grown from a solution or from a vapour phase, and may grow suspended in the growth medium or grow in contact with a substrate.

The VLS mechanism is the most widely cited growth method. The VLS mechanism was originally proposed by Wagner and Ellis [11] in 1964 to explain the anisotropic growth of Si wires catalysed by metallic Au particles. The VLS mechanism, so-called due to the vapour, liquid and solid phases involved, is schematically illustrated in Fig. 2.1. The Si precursor species were supplied in the *vapour* phase. At growth temperature the metallic Au particle formed a *liquid* eutectic alloy with the Si. With further supply of Si this Au–Si alloy particle became supersaturated with Si, and the Si precipitated at the particle–semiconductor interface to form a *solid* crystalline Si wire. Wagner and Ellis proposed two possibilities to explain nanowire growth. First, that due to the high accommodation coefficient of the liquid phase, the liquid particles are favourable collection sites for the vapour phase reaction species, and thus assist nanowire growth. The second possibility is that the metallic particle is a chemical catalyst which lowers the activation energy barriers to enhance the decomposition of the gas-phase precursors [13].

Following work on Si wire growth, Hiruma et al. [14] applied the same principle to grow III–V nanowires. Hiruma et al. [14] used Au nanoparticles to direct III–V nanowire growth via a VLS-like mechanism. We refer to this nanowire growth process as “Au-assisted”, as coined by Dick et al. [15].

For III–V nanowires, this Au-assisted nanowire growth mechanism lends itself to a number of standard industrial and laboratory growth systems, including laser-assisted catalytic growth [16], molecular beam epitaxy (MBE) [17], chemical beam epitaxy (CBE) [18], and metalorganic chemical vapour deposition (MOCVD) [19,20]. Of all these techniques, the most promising and most common technique for III–V nanowire growth is MOCVD. This approach achieves epitaxial nanowires that are free-standing on the growth substrate, offers great flexibility and high accuracy in nanowire design, and is readily scalable for industrial mass fabrication. The growth parameters can be tightly controlled to achieve the desired material properties. Indeed, Au-assisted MOCVD growth has produced nanowires with abrupt heterostructure interfaces, high purity, controlled doping, and perfect phase purity. For these reasons, Au-assisted MOCVD is our method of choice for III–V nanowire device fabrication.

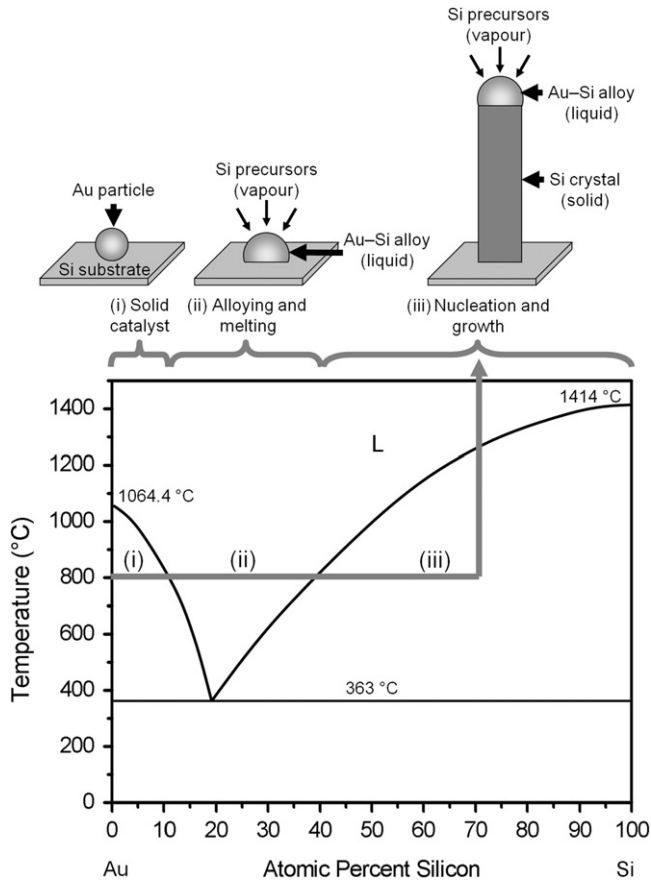


Fig. 2.1. Schematic illustration of the VLS growth of Si wires using an Au catalyst particle. The Au–Si binary phase diagram illustrated in the lower portion indicates the various phases the Au–Si particle can adopt under different temperatures and in different composition ranges. The grey arrow, and labels (i), (ii) and (iii) illustrate the different stages of nanowire growth for a growth temperature of 800 °C, and the corresponding state of the Au–Si particle.

### 3. Fundamental principles of III–V nanowire growth by Au-assisted MOCVD

#### 3.1. Basic growth mechanism

The Au-assisted MOCVD growth mechanism is closely related to, if not identical to, the VLS growth mechanism discussed above. We outline the basic mechanism of III–V nanowire growth by Au-assisted MOCVD with reference to the schematic illustration of Fig. 3.1. Initially, Au nanoparticles are deposited on a semiconductor substrate surface, as in Fig. 3.1a. To initiate growth, vapour phase group III and group V precursors are provided to the reaction chamber. During growth, these precursors pyrolyse (decompose) to yield group III and group V elements.

Deposition of III–V material occurs preferentially at the nanoparticle–substrate interface, so that nanowire nucleation takes place (Fig. 3.1c). With continual supply of

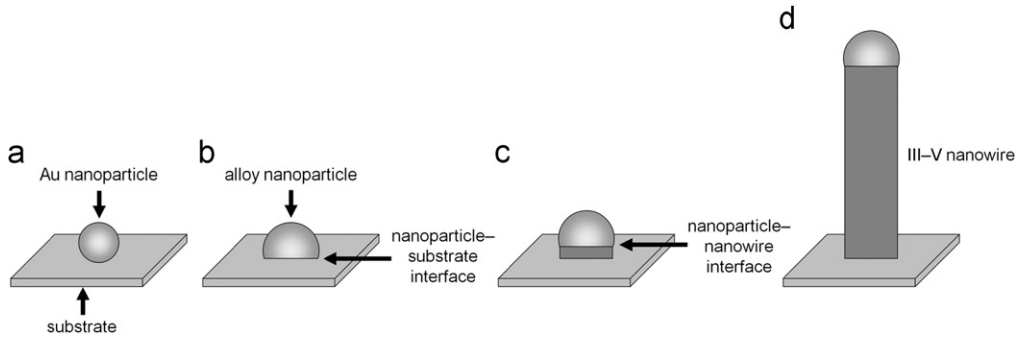


Fig. 3.1. Schematic illustration of the nanowire growth mechanism: (a) Au nanoparticles are deposited on the semiconductor substrate; (b) vapour phase reactants are supplied and the nanoparticle alloys with specific reactant elements; (c) nucleation takes place at the nanoparticle-substrate interface and (d) growth continues at the nanoparticle-nanowire interface.

group III and V reactants, deposition of III–V material continues at the nanoparticle–nanowire interface. Thus the nanoparticle, located at the growing tip of the nanowire, drives highly anisotropic nanowire growth (Fig. 3.1d). The diameter at the tip of the grown nanowire is governed by the diameter of the Au nanoparticle. The following sections describe the growth process in further detail. This is essentially a bottom-up fabrication technique which offers high controllability in nanoscale dimensions not possible by top-down techniques.

### 3.2. Growth procedure

In our MOCVD system, group III elements, Ga, In and Al, and group V element, Sb, are supplied as vapour phase organometallic precursor species: trimethylgallium ( $\text{Ga}(\text{CH}_3)_3$ , TMGa), trimethylindium ( $\text{In}(\text{CH}_3)_3$ , TMIIn), trimethylaluminium ( $\text{Al}(\text{CH}_3)_3$ , TMAI), and trimethylantimony ( $\text{Sb}(\text{CH}_3)_3$ , TMSb), respectively. Group V elements As and P are supplied as vapour phase hydrides: arsine ( $\text{AsH}_3$ ) and phosphine ( $\text{PH}_3$ ), respectively. These reactants are carried into the reactor by ultra-high purity hydrogen gas,  $\text{H}_2$ . During growth, these precursors pyrolyse to release group III and group V elements. A number of reports describe precursor pyrolysis in detail [21,22].

In our laboratory, (1 1 1)B-oriented III–V substrates, such as GaAs and InP, are used for nanowire growth. Typically, nanowires are grown on substrates of the same material, for instance GaAs nanowires are grown on GaAs substrates. Before growth, Au nanoparticles are deposited on the substrate surface, as will be described in Section 5.1. The prepared substrate, hosting deposited Au nanoparticles, is placed into the reactor on a graphite susceptor. The substrate is heated to  $600^\circ\text{C}$  and annealed in situ for 10 min to desorb surface contaminants, including the surface oxide. Annealing is performed under group V overpressure to prevent decomposition of the substrate.

After annealing, the substrate is cooled to growth temperature, typically between  $350$  and  $550^\circ\text{C}$ . The group V flow rate is adjusted for growth. Then group III precursors are fed to the reaction chamber to initiate growth. Growth times are generally between 30 s and 120 min, chosen according to the growth rate and the desired nanowire length. Upon completion of growth, the samples are cooled under group V overpressure.



All samples were grown with a reactor pressure of 100 mbar and a total gas flow rate of 15 standard L/min.

### 3.3. Alloying of the Au nanoparticle

During the annealing and growth processes, the Au nanoparticle alloys with specific group III and group V elements to form a liquid or solid alloy, for instance Au–Ga (Fig. 3.1b). The alloying behaviour is significantly more complex than for Au-assisted Si wires (as described in Section 2.2), because at least three different elements are involved: Au, a group III and a group V. Binary and ternary phase diagrams [23–32] indicate which alloy phases are stable at room temperature, during annealing and at growth temperature. At typical nanowire growth temperatures (between 350 and 550 °C), Al, Ga, In and Sb can each alloy with Au to produce eutectic liquid or stable solid alloys [23–27]. On the other hand, P and As are not thought to alloy significantly: the Au–As phase diagram does not include any intermetallic solid phases, the only solid Au–P phase is metastable, the solubility of As and P in solid Au is low, and typical nanowire growth temperatures are too low to form eutectic liquid Au–As or Au–P alloys [28,29]. Dick et al. [33] have published a thorough account of the possible alloy phases of the nanoparticle during growth.

Even with the assistance of binary and ternary phase diagrams, it is difficult to ascertain the exact phase, solid or liquid, of the nanoparticle during growth. Firstly, most phase diagrams were derived for atmospheric pressure rather than the low reactor pressures typically used for nanowire growth. Secondly, size-dependent melting effects limit the applicability of bulk phase diagrams. The small scale of the alloyed Au nanoparticles makes them subject to size-dependent melting effects, according to the Gibbs–Thomson relation. Therefore, the melting point of the alloy nanoparticles may be depressed relative to the bulk melting point, so eutectic melting may occur at a lower temperature than the bulk phase diagrams predict. A further factor is melting–freezing hysteresis observed for alloyed nanoparticles [34,35].

Thirdly, the composition of the particle, when analysed post-growth, is generally different to that during growth. After growth is complete, the group III flow is ceased and the sample is cooled under group V overpressure. This high group V vapour supersaturation continues to drive the III–V growth reaction which consumes group III species alloyed within the nanoparticle. Thus during cooling, III–V material continues to deposit at the nanoparticle–nanowire interface and group III species in the Au particle are depleted. Several studies have compared the nanoparticle composition after different cooling procedures, to determine the nanoparticle phase during growth [36,37].

Doubt about the physical state of the particle, whether liquid or solid, has created doubt about whether the growth mechanism is truly VLS. A vapour–solid–solid (VSS) mechanism in which the nanoparticle is solid, has been proposed [15,36,38]. In situ TEM growth studies have observed both VLS and VSS mechanisms, and have demonstrated that growth is more rapid when the nanoparticle is liquid [39]. According to the conventional VLS and VSS mechanisms, reaction species dissolve into the nanoparticle and are transported to the growth interface via bulk diffusion through the nanoparticle. The elements with high solubility in Au (Al, Ga, In, Sb) are assumed to travel to the interface by bulk diffusion through the nanoparticle, whereas the elements with low solubility (As, P) are thought to arrive at the growth interface directly from the vapour, without dissolving into the nanoparticle. In this case, As and P would be incorporated at the three phase contact line



where vapour, nanoparticle and nanowire meet. Another strong possibility is that reactants are transported to the growth interface by diffusing on the nanoparticle surface, rather than by diffusing through the nanoparticle interior [40].

Recently, the theory of preferential interface nucleation (PIN) has been proposed as the fundamental mechanism underpinning the VLS mechanism and variations such as the VSS mechanism and the solution–liquid–solid mechanism [41]. According to the PIN theory, the probability of nucleation is highest at the nanoparticle–semiconductor interface and this drives nanowire growth. A comprehensive review article by Dick [22] describes recent progress towards understanding the mechanism of Au-assisted nanowire growth.

Despite these controversies, the general principle of Au-assisted nanowire growth remains: the nucleation rate is highest at the Au nanoparticle–semiconductor interface, which drives nanowire growth.

### 3.4. Axial and radial growth modes

There are two major growth modes taking place during Au-assisted nanowire growth by MOCVD: axial growth and radial growth.

Axial growth is the term describing the Au-assisted elongating growth of the nanowire. There are two major contributions to axial nanowire growth, as illustrated in Fig. 3.2a. The first contribution is from reaction species which directly impinge on the nanoparticle. The second contribution arises from species adsorbed on the substrate or nanowire sidewalls. These adatoms (adsorbed atoms) diffuse along the concentration gradient towards the Au nanoparticle, where they are incorporated into axial growth. Surface diffusion is more significant for group III adatoms, which have large diffusion lengths ( $\lambda$ ),

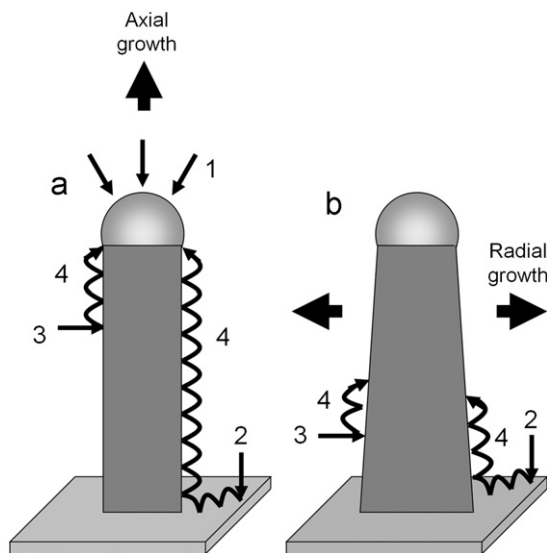


Fig. 3.2. Schematic illustration of adatom contributions to (a) axial growth and (b) radial growth. The adatom contributions include those (1) directly impinging on the Au nanoparticle and those adsorbed on the (2) substrate and (3) nanowire sidewalls which (4) diffuse along the concentration gradient towards the nanoparticle–nanowire interface.

whereas group V adatoms have much smaller diffusion lengths. Group V species have significantly lower diffusivity, and are believed to incorporate close to the position of adsorption.

Johansson et al. [42] have developed a theoretical model describing the dependence of the axial growth rate on the diffusion length on the substrate ( $\lambda_s$ ) and nanowire sidewalls ( $\lambda_w$ ). The diffusion of adatoms gives rise to some interesting nanowire growth results. One of these results is density dependence. In regions of high nanowire density, adjacent nanowires spaced within a diffusion length,  $\lambda_s$ , compete for diffusing adatoms. As a result, nanowires in high density regions may feature slower axial growth rates than those in low density regions [43]. Another report by Dayeh et al. [44] describes two different growth regimes, defined by whether  $\lambda_s$  or  $\lambda_w$  is larger, which lead to time-varying growth rates.

Radial growth, also known as lateral or conformal growth, is the deposition of material on the nanowire sidewalls. It follows a simple vapour–solid growth mechanism, and does not directly involve the Au nanoparticle. As illustrated in Fig. 3.2b, radial growth occurs when species adsorbed on the substrate and nanowire sidewalls, diffuse and incorporate on the nanowire sidewalls. In this manner, radial growth competes with axial growth.

Tapered nanowire morphologies, whereby nanowires exhibit wider bases and taper to narrower Au-capped tips, are a consequence of radial growth, as explained here. Nanowire bases are grown first, and hence are exposed to reactants for longer than the more recently grown Au nanoparticle-capped tip. Also, owing to their proximity to the substrate, the nanowire bases receive a greater fraction of precursor materials collected on and diffusing from the substrate [45]. Thus, lower sections of the nanowire experience more radial growth, which leads to tapered nanowire morphologies with wider bases and narrower tips as illustrated in Fig. 3.2b.

A further growth process is the deposition of planar layers on the substrate surface. This occurs when adatoms incorporate onto the substrate, rather than onto the nanowire sidewalls or nanowire tip.

#### 4. Nanowire morphology and crystal structure

Field emission scanning electron microscopy (FESEM) is used to identify general nanowire morphology, including facet planes, diameter and height. Typically, the FESEM is operated at low acceleration voltages, generally 3 kV. In Fig. 4.1a and b, we illustrate FESEM images of typical GaAs and InAs nanowires grown via Au-assisted MOCVD. The nanowires are vertically aligned on their (1 1 1)B terminated substrates indicating their epitaxial relationship with the substrate. The [1 1 1]B direction is the energetically preferred growth direction. These nanowires are tapered with narrow tips and wider bases. At the tip of each nanowire lies an Au alloy nanoparticle which drives nanowire growth.

##### 4.1. Nanowire crystal structure

Transmission electron microscopy (TEM) is used to determine crystallographic properties and further elucidate nanowire structure. III–V nanowires can adopt either a cubic zinc-blende (ZB) structure or hexagonal wurtzite (WZ) structure. The WZ structure has been reported, for instance, in MOCVD-grown InP nanowires [46] and in MBE-grown

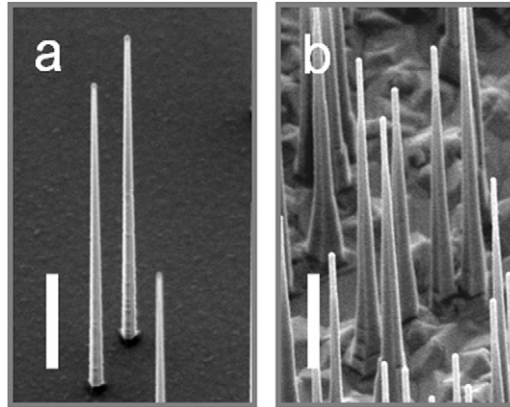


Fig. 4.1. FESEM images of (a) GaAs nanowires on a GaAs (1 1 1)B substrate and (b) InAs nanowires on an InAs (1 1 1)B substrate. These wires were grown using 50 nm diameter Au nanoparticles. Samples are tilted at 40°. Scale bars are 1  $\mu\text{m}$ .

GaAs nanowires [47]. The ZB structure is common in MOCVD-grown GaAs and GaP nanowires [48,49].

ZB and WZ crystal structures can have very different optical and electrical properties, so the distinction is significant. The difference between ZB and WZ crystals lies in the stacking of the bilayers composing the crystal. ZB lattices follow an ABCABC stacking sequence and WZ lattices follow an ABABAB stacking sequence, where each letter represents a bilayer of III–V pairs.

There are certain types of planar defects which commonly occur in nanowires: twin planes and stacking faults. Twin planes occur when a single bilayer is faultily stacked in a ZB crystal, which reverses the stacking sequence from ABC to CBA. For instance, in the sequence ABCACBA, *C* is the faultily stacked bilayer which creates the twin plane. The crystal on one side of *C* is rotated 60° about the [1 1 1]B growth axis relative to the crystal on the opposite side. Stacking faults in WZ structures occur when a single bilayer is misplaced, for instance, the sequence ABACACA contains a stacking fault at bilayer *C*. A WZ structure is equivalent to a ZB structure with a twin plane every bilayer. The crystal structure of the nanowires, including the density of planar crystallographic defects, is determined by the growth parameters, as will be discussed later.

With TEM, nanowire crystal structure is routinely determined by tilting the nanowire to the  $\langle 1 \bar{1} 0 \rangle$  zone axis. This allows ZB phases, WZ phases, twin defects and stacking faults to be distinguished. All TEM results presented in this review were taken along the  $\langle 1 \bar{1} 0 \rangle$  zone axis.

#### 4.2. Nanowire side facets

III–V nanowires also exhibit side facets of different orientations. WZ nanowires form a hexagonal prism with either six  $\{1 1 \bar{2} 0\}$  side facets, or six  $\{1 \bar{1} 0 0\}$  side facets, as shown in Fig. 4.2a and b. The  $\{1 1 \bar{2} 0\}$  and  $\{1 \bar{1} 0 0\}$  surfaces are non-polar, and consequently the nanowire cross-section is hexagonal with six faces of equal length. ZB nanowires can

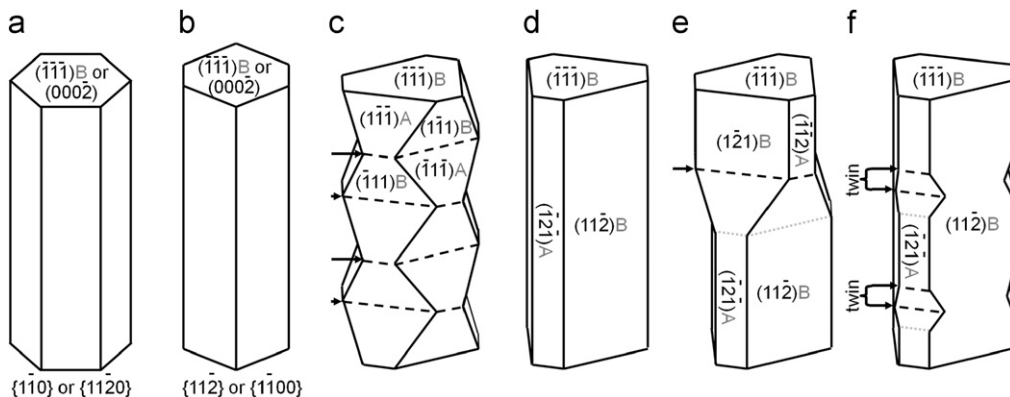


Fig. 4.2. Schematic illustration of possible nanowire morphologies. Polar facets are labelled as “A” or “B” in faint font. (a) Hexagonal cross-section with six  $\{1\bar{1}0\}/\{11\bar{2}0\}$  side facets. (b) Hexagonal cross-section with six  $\{11\bar{2}\}/\{1\bar{1}00\}$  side facets. (c) Octahedral segments with  $\{111\}_A$  and B faces. The dotted lines with arrows indicate twin planes. (d) Near triangular cross-section with three dominant  $\{112\}_B$  facets and three smaller  $\{112\}_A$  facets. (e) Effect of a single twin plane on nanowire morphology. The triangular segment above the twin plane is rotated  $60^\circ$  about the growth axis, relative to the triangular segment below the twin. (f) Effect of a thin twinned segment on nanowire morphology. The twinned segment is bounded by the curly braces. The twinned segment creates a groove flanked by the adjacent  $\{112\}_A$  facets.

exhibit a wider range of morphologies. ZB nanowires can be composed of octahedral segments, each with three  $\{111\}_A$  and three  $\{111\}_B$  side facets [49]. Each octahedral segment is bounded by a twin plane above and a twin plane below, such that each octahedral segment has a crystal structure rotated  $60^\circ$  about the  $[111]_B$  growth axis compared to the adjacent segments. This structure is illustrated in Fig. 4.2c. Like WZ nanowires, ZB nanowires can have hexagonal cross-sections with either six  $\{1\bar{1}0\}$  or six  $\{11\bar{2}\}$  side facets, as shown in Fig. 4.2a and b. Note that the  $\{1\bar{1}0\}$  and  $\{11\bar{2}\}$  families are parallel, and the  $\{11\bar{2}\}$  and  $\{1\bar{1}00\}$  families are also parallel.

The  $\{11\bar{2}\}/\{1\bar{1}0\}$  and  $\{1\bar{1}00\}$  faces are non-polar, whereas the six  $\{11\bar{2}\}$  facets are not all equivalent, and can be subdivided into three  $\{112\}_A$  and three  $\{112\}_B$  faces. The  $\{112\}_A$  faces consist of two threefold coordinated group III surface atoms and one twofold coordinated group V surface atom in each surface unit cell, and the  $\{112\}_B$  faces consist of two threefold coordinated group V surface atoms and one twofold coordinated group III surface atom in each surface unit cell. Due to the differences in surface stoichiometry, group III atoms attach preferentially to  $\{112\}_A$  surfaces. Under growth conditions of high group V overpressure, the  $\{112\}_B$  facets are more stable with a lower surface energy and a slower growth rate than the  $\{112\}_A$  facets. Radial growth occurs preferentially on the  $\{112\}_A$  surfaces, and the remaining  $\{112\}_B$  facets become elongated as the  $\{112\}_A$  surfaces grow out. Consequently, the cross-section adopts a truncated triangular shape with elongated  $\{112\}_B$  side facets and shorter  $\{112\}_A$  side facets, as illustrated in Fig. 4.2d [48,50].

In the case of these  $\{112\}$  faceted triangular nanowires, the overall morphology is further modified by the presence of twin planes. When a twin plane forms, the crystal structure is rotated  $60^\circ$  about the  $[111]_B$  growth axis. This means that the section of nanowire below the twin exhibits a triangular cross-section oriented one way, and the section of nanowire above the twin exhibits a triangular cross-section oriented the opposite

way, as illustrated in Fig. 4.2e. Finally, if a thin twinned segment is inserted into a perfect crystal region, it creates a groove between the  $\{1\ 1\ 2\}$ A sidewalls flanking the twinned segment, as illustrated in Fig. 4.2f. The groove forms there, because there the twinned segment presents a slow-growing  $\{1\ 1\ 2\}$ B sidewall, not a  $\{1\ 1\ 2\}$ A sidewall like those flanking the twinned segment. As a result the nanowire structure resembles a stack of truncated triangles [48].

The above discussion has focused the formation of elongated  $\{1\ 1\ 2\}$ B facets under high group V overpressure. Under growth conditions of low group V overpressure, the situation can reverse so that  $\{1\ 1\ 2\}$ A facets become more elongated [50].

## 5. Tailoring nanowire growth

In MOCVD, a number of growth parameters can be accurately tuned to grow high quality nanowires suitable for device applications. To a first approximation, the *diameter* at the tip of the nanowire is determined by the catalyst diameter. Other nanowire properties, such as *height*, *morphology*, *crystal structure*, *crystallographic defects* and *impurity incorporation* can be tailored by choosing appropriate growth parameters. These include growth time, temperature, pressure and the flow rates of group III and group V precursors [51–53].

The focus of this section is tailoring the MOCVD growth of III–V nanowires, using GaAs nanowires as the primary example. The GaAs nanowires presented in this section were grown on GaAs (1 1 1)B substrates using TMGa and AsH<sub>3</sub> precursors.

### 5.1. Substrate preparation

First, we compare different methods of substrate preparation to obtain high quality III–V nanowires. One method is to deposit a thin 1–10 nm layer of Au on the substrate via thermal or electron beam evaporation. Upon annealing, the layer breaks apart into small Au droplets whose size depends on the annealing temperature and whose density depends on the layer thickness. This method is simple but it is difficult to obtain a uniform nanoparticle size or distribution. Alternatively, Au nanoparticles can also be sourced as size-selected aerosol particles, or, as routinely used in our laboratory, Au colloid nanoparticles within solution (British Biocell International–Ted Pella Inc.). Each solution contains monodisperse Au nanoparticles of a given diameter and density. The colloidal Au nanoparticles carry a net negative surface charge so that Coulombic repulsion prevents nanoparticle agglomeration in solution. Due to their net negative charge, the nanoparticles do not naturally adhere to III–V substrates. In the laboratory, these colloidal Au nanoparticles may be deposited on a III–V substrate by one of the three possible methods: (i) evaporation, (ii) poly-L-lysine (PLL), and (iii) hydrochloric acid (HCl).

For method (i) a 100  $\mu$ L droplet of Au colloidal solution is applied to the substrate and allowed to evaporate. To obtain a reasonable density of deposited Au, the colloidal solution is diluted to approximately  $10^9$  nanoparticles/mL before it is applied. This method is simple, but during the evaporation process the Au nanoparticles tend to agglomerate and deposit non-uniformly.

Method (ii) involves functionalising the substrate with PLL before applying colloidal Au. The substrate is first immersed in 0.1% PLL solution for 60 s, then rinsed with deionised (DI) water, and dried with nitrogen, N<sub>2</sub>. Then, a 100  $\mu$ L droplet of Au colloidal

solution is dispersed on the substrate, and rinsed away with DI water after a contact time of 5–30 s, and the substrate is again dried with  $N_2$ . A longer contact time is used for lower density Au colloidal solutions, to achieve a sufficient density of Au nanoparticles adhering to the substrate surface. PLL is a positively charged polyelectrolyte which attracts the negatively charged Au nanoparticles and immobilises them on the substrate surface. This PLL functionalisation–Au nanoparticle deposition method prevents agglomeration of nanoparticles during deposition and achieves an even distribution on the substrate. Treatment with polyamines, such as PLL, is widely used in the life sciences to immobilise cells on slides, and also has been used to immobilise nanoparticles to create standard samples for atomic force microscope calibration [54]. The resulting nanowires are shown in Fig. 5.1a.

Method (iii) involves dispensing a 100  $\mu\text{L}$  droplet of Au colloidal solution on the substrate. Then, a 50  $\mu\text{L}$  droplet of 0.03 M HCl is added to the Au colloid droplet and allowed to mix on the substrate for 10 s. The resulting HCl concentration is 0.01 M. The substrate is rinsed with DI water and dried with  $N_2$ . This method was developed by Woodruff et al. [55] for deposition of Au colloids on Si substrates using HF instead of HCl. When the acid is added to the Au colloid droplet, the droplet pH is lowered, the negative charge on the Au nanoparticles is neutralised, and the nanoparticles can attach to the substrates. Fig. 5.1b shows nanowires grown on substrates prepared by this method.

The optimum method, which affords control over both nanoparticle size and distribution, is patterning of Au nanoparticles using electron beam lithography (EBL). This technique is time-consuming and requires complex EBL processing. The PLL functionalisation–Au colloid deposition process, used routinely in this work, is suitable for most device applications and is ideal for research into nanowire growth processes. It is suitable for all substrates used, including III–V substrates and the quartz substrates used

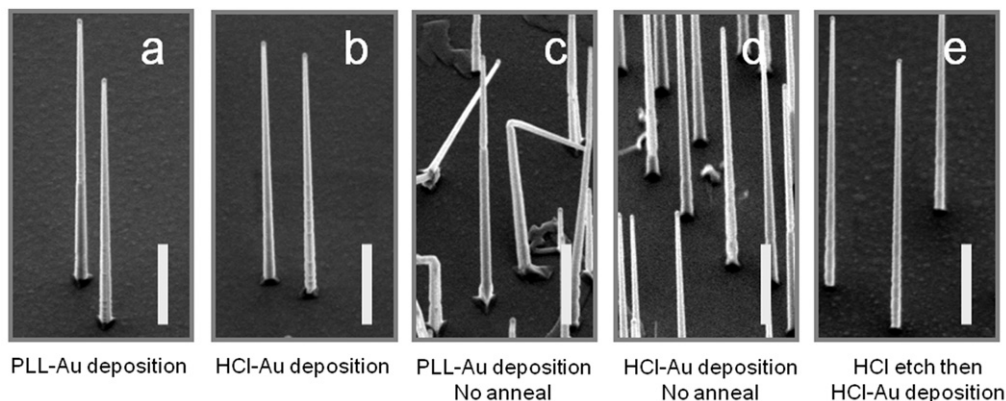


Fig. 5.1. FESEM images of GaAs nanowires grown on GaAs substrates prepared by different methods: (a) substrate prepared by the PLL method (method (ii)), involving PLL functionalisation followed by colloidal Au deposition, followed by an in situ annealing step prior to nanowire growth; (b) substrate prepared by the HCl method (method (iii)), involving deposition of HCl and Au colloidal solutions, followed by an in situ annealing step prior to nanowire growth; (c) substrate prepared using the PLL (method (ii)) but without any in situ annealing step; (d) substrate prepared using the HCl (method (iii)) but without any in situ annealing step and (e) substrate etched in 1 M HCl, prior to treatment with the HCl method (method (iii)). Scale bar is 1  $\mu\text{m}$ .



for TCS measurements. Unless otherwise stated, all samples presented in this article were prepared using PLL functionalisation, followed by Au colloid deposition.

Before growth, the substrates are annealed in situ, as described in Section 3.2. The annealing step removes the surface oxide and other contaminants. In Fig. 5.1 the effect of the annealing step is clear from comparing parts a and b, where growth was performed with a pre-growth annealing, against parts c and d, where growth was performed without a pre-growth annealing step. Nanowire growth is more irregular in parts c and d, presumably because surface roughness and contaminants remaining on the unannealed surface hinder the nucleation of straight epitaxial nanowires. The similarity between the PLL and HCl treated samples indicates that PLL functionalisation does not interfere significantly with nanowire growth. PLL and HCl treatments were also compared for InAs substrates with InAs nanowires, and the two treatments gave identical results.

This annealing step means that the III–V substrates do not require etching or cleaning before growth. Etching to remove the surface oxide, prior to Au nanoparticle deposition, was performed for the sample of Fig. 5.1e. To etch the substrate, it was immersed in 1 M HCl for 2 min, rinsed with DI water and dried with  $N_2$ . We found that etching did not have any measurable effect on the properties of the grown nanowires. As seen in Fig. 5.1 by comparing part a (or b) with part e, the resulting nanowire properties are comparable regardless of etching.

## 5.2. Effects of growth temperature

Growth temperature has a marked effect on nanowire properties. Fig. 5.2 illustrates the morphological changes that take place with different growth temperatures. In Fig. 5.2a and b, we note that temperature increases both axial and radial growth rates, so that nanowires are taller and have wider bases. This occurs because, as temperature is increased, the rate of precursor decomposition increases and the adatom diffusion length increases. More Ga adatoms are available for both axial and radial growth.

As temperature is increased beyond 450 °C (Fig. 5.2b and c), however, only the radial and planar growth rates continue to increase and the axial growth rate decreases. This occurs because the increasing radial growth and planar growth compete with axial growth

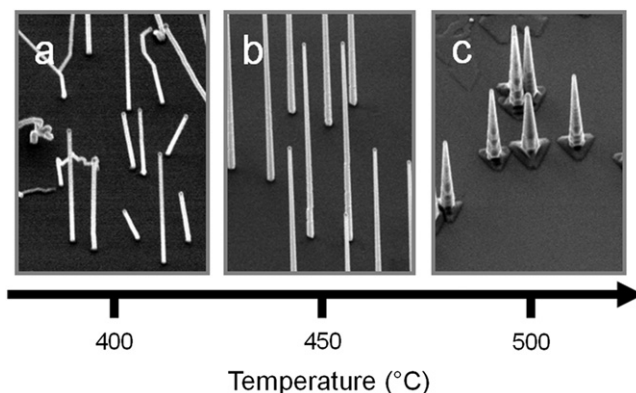


Fig. 5.2. FESEM images of GaAs nanowires grown at growth temperatures of: (a) 425 °C, (b) 450 °C and (c) 475 °C. Samples are tilted at 40°. Scale bar is 1  $\mu$ m.



for diffusing adatoms. This competing growth depletes the nanoparticle–nanowire interface of Ga adatoms diffusing from the substrate and along nanowire sidewalls, and consequently axial growth decreases. Consequently, at the highest growth temperatures (Fig. 5.2c), the nanowires are short and suffer severe tapering.

Tapering is undesirable for many device applications, including lasers, where a uniform diameter is required. Tapering can be minimised by using a low growth temperature. However, at the lower growth temperatures of 400 °C and below, nanowire growth is kinked and irregular, as illustrated in Figs. 5.2a and 5.3a. Rather than following a  $[1\ 1\ 1]_{\text{B}}$  growth direction, these nanowires initiate in non- $[1\ 1\ 1]_{\text{B}}$  directions and continue to kink and grow irregularly. This irregular growth may be caused by a number of possible factors, including partial or complete solidification of the nanoparticle at low temperature, or an unfavourable surface reconstruction of the  $[1\ 1\ 1]_{\text{B}}$  surface at low temperature [51].

We devised a two-temperature procedure to access growth temperatures as low as 350 °C without the nanowires kinking. In the procedure, growth was initiated with a brief high temperature nucleation step of approximately 1 min at a nucleation temperature,  $T_{\text{n}}$ , of 450 °C. Following this nucleation step the temperature was rapidly ramped down to a growth temperature,  $T_{\text{g}}$ , between 350 and 400 °C while growth continued. Prolonged growth then took place at  $T_{\text{g}}$ . The high temperature nucleation step prevents kinking, possibly by melting the nanoparticle at  $T_{\text{n}}$  so that the nanoparticle remains a supercooled liquid even after cooling to the low  $T_{\text{g}}$  (due to melting–freezing hysteresis), or possibly by stabilising a favourable surface reconstruction of the  $[1\ 1\ 1]_{\text{B}}$  surface. The resulting nanowires are straight,  $[1\ 1\ 1]_{\text{B}}$  oriented, and minimally tapered owing to the low growth temperature.

A lower growth temperature has a further advantage: it dramatically decreases the density of twin defects in these ZB nanowires. Fig. 5.4 compares TEM images of a twinned GaAs nanowire grown by the single temperature procedure with  $T_{\text{g}}$  of 450 °C (part a) and a twin-free GaAs nanowire grown by the two-temperature procedure with  $T_{\text{g}}$  of 375 °C (part b).

Finally, the low growth temperature dramatically improves the nanowire optical properties. For PL measurements, the nanowires were clad in AlGaAs shells and a GaAs capping layer (to be discussed in Section 7.2). Nanowires grown at low temperature

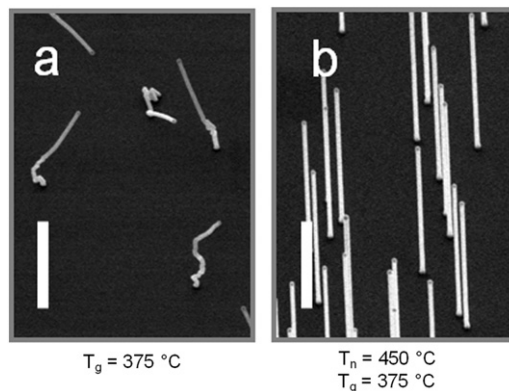


Fig. 5.3. FESEM images of GaAs nanowires grown (a) at a single temperature of 375 °C and (b) by the two-temperature procedure, with nucleation step at 450 °C and growth step at 375 °C. Scale bar is 1  $\mu\text{m}$ .

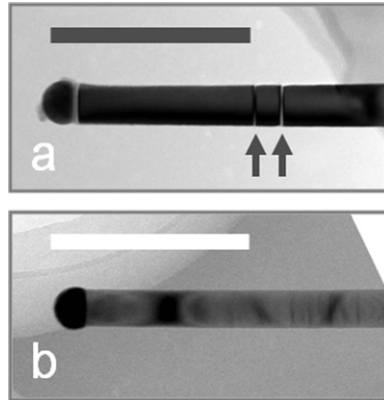


Fig. 5.4. Bright field TEM images of (a) twinned nanowires grown at a high temperature of 450 °C and (b) twin-free nanowires grown at a low temperature of  $T_g = 375$  °C. The nanowires of (b) were grown via the two-temperature procedure with a nucleation step at  $T_n = 450$  °C. Arrows indicate twin defects. Scale bars are 250 nm. Reproduced with permission from [51].

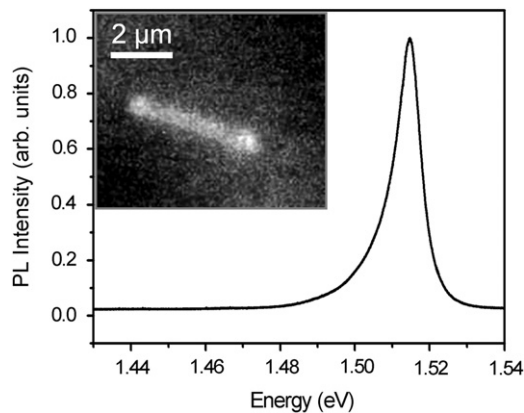


Fig. 5.5. PL spectrum of an ensemble of nanowires grown at  $T_g = 375$  °C. The nanowires were grown via the two-temperature procedure with a nucleation step at  $T_n = 450$  °C. The inset is a micro-PL image of one of these nanowires.

( $T_n$  of 450 °C and  $T_g$  of 375 °C) exhibited a strong PL peak at 1.518 eV, corresponding to exciton recombination. This PL could be imaged at room temperature, whereas PL from the high temperature grown wires was too weak to be imaged successfully (Fig. 5.5). The exciton lifetime, of approximately 1 ns, was considerably longer than that measured for the high temperature grown nanowires [56]. This will be further discussed in Section 8.5.

### 5.3. Effects of V/III ratio

Another key parameter is the V/III ratio, that is, the ratio of the group V precursor flow rate relative to the group III precursor flow rate. GaAs nanowires were grown with a control TMGa flow of  $\text{III}_0 = 1.2 \times 10^{-5}$  mol/min, and  $\text{AsH}_3$  flow rates between  $1.3 \times 10^{-4}$  and  $2.1 \times 10^{-3}$  mol/min to attain V/III ratios of 12, 23, 46, 93 and 190. Adjunct studies

were performed with other TMGa flow rates of  $\frac{1}{4}\text{III}_0$ ,  $\frac{1}{2}\text{III}_0$ ,  $2\text{III}_0$  and  $\text{III} = 4\text{III}_0$ . In each study, TMGa was held constant and the  $\text{AsH}_3$  flow was chosen to achieve a given V/III ratio. Varying the  $\text{AsH}_3$  flow is notionally equivalent to varying the V/III ratio.

The V/III ratio has a pronounced effect on nanowire morphology, as detailed in the FESEM images of Fig. 5.6. At lower V/III ratios, nanowires are regular and growth occurs in the vertical  $[1\ 1\ 1]\text{B}$  direction. Both the axial growth and radial growth rates increase with increasing  $\text{AsH}_3$  flow. This is expected, because a high V/III ratio decreases the activation energy for GaAs growth, so a higher V/III ratio increases the axial and radial growth rates. At a critical V/III ratio the growth rate reaches a maximum. This critical V/III ratio is approximately 40, for all III flows investigated. Beyond this, the growth rate ceases to increase, and instead drops significantly. It is thought that at high V/III ratios, stable As trimers can form on  $\{1\ 1\ 1\}\text{B}$  surfaces. This As trimer surface reconstruction hinders growth. Thus, the axial growth rate decreases at the highest V/III ratios.

At higher V/III ratios, some nanowires kink to non-vertical orientations, and the proportion of these kinked irregular nanowires increases with V/III ratio. This critical V/III ratio was approximately 90, for all III flows investigated. Furthermore, nanowires appear more tapered at the highest V/III ratios, due to the increase in radial growth rate coupled with the decrease in axial growth rate.

The crystal properties are also affected by V/III ratio. Notably, increasing the  $\text{AsH}_3$  flow, and hence increasing the V/III ratio, decreases the density of twin defects in these ZB structures. The excess As is thought to decrease surface and interfacial energies in the nanoparticle–nanowire system, and thus stabilise the ZB structure while hindering twin defect formation.

PL measurements reveal the effect of V/III ratio on nanowire optical properties. In Fig. 5.7a we plot the PL spectra of three samples grown with different V/III ratios. The peak at 1.518 eV is characteristic of free exciton recombination in GaAs. The lower energy peak arises from donor–acceptor-pair (DAP) recombination involving a neutral donor and a neutral carbon acceptor ( $\text{D}^0$ ,  $\text{C}_{\text{As}}$ ). Identification of this peak will be discussed in Section 8.5. The relative intensity of the DAP peak to the exciton peak indicates the degree of C impurity incorporation. In Fig. 5.7a, the DAP peak intensity decreases with increasing V/III ratio, indicating that C impurity incorporation decreases as V/III ratio is increased. This is explained as follows. C impurities arise from methyl ( $\text{CH}_3$ ) radicals

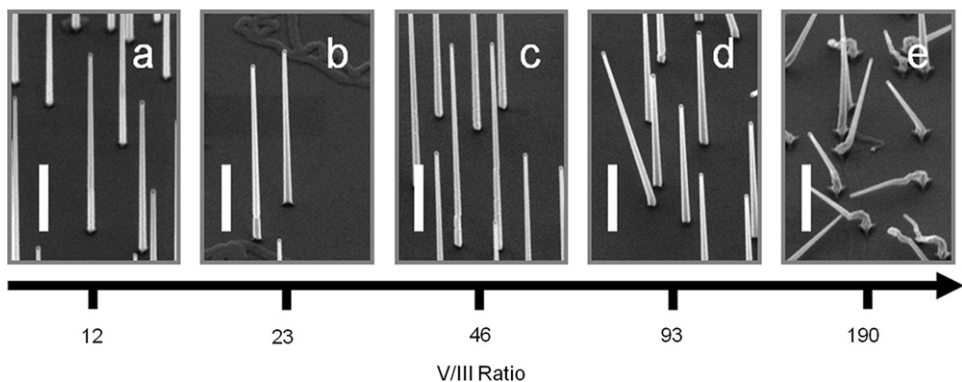


Fig. 5.6. FESEM images of GaAs nanowires grown at constant group III flow rate of  $\text{III} = \text{III}_0$  and the indicated V/III ratios: (a) 12, (b) 23, (c) 46, (d) 93 and (e) 190. Samples are tilted at  $40^\circ$ . Axis is logarithmic. Scale bars are  $1\ \mu\text{m}$ . Reproduced with permission from [52].

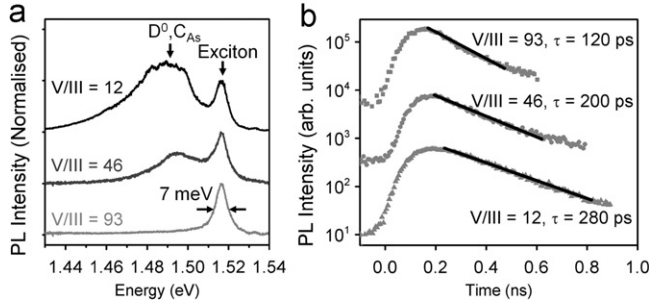


Fig. 5.7. (a) PL spectra comparing the relative intensities of DAP and exciton emission. The spectra were taken from nanowire ensembles grown at various V/III ratios (V/III = 12, 46 and 93) with constant III flow (III = III<sub>0</sub>). The bottommost spectrum features a FWHM of only 7 meV. Spectra are normalised to the exciton peak at 1.518 eV. Spectra are offset for clarity. (b) Time decays of the exciton (at 1.518 eV) taken from nanowires grown at different V/III ratios. Decays are offset for clarity. Reproduced with permission from [52,53].

adsorbed on the surface during the decomposition of TMGa. AsH<sub>3</sub> suppresses the adsorption of these methyl radicals, as AsH<sub>3</sub> pyrolysis produces atomic hydrogen which bonds with the CH<sub>3</sub> radicals to produce volatile methane (CH<sub>4</sub>) reaction products, and then removes the C bearing radical from the growth surface. Thus, higher AsH<sub>3</sub> flow rates, or equivalently higher V/III ratios, reduce C incorporation [52].

Finally, time-resolved PL measurements indicate that V/III ratio has a deleterious effect on exciton lifetime,  $\tau$ . Fig. 5.7b shows time decays of the exciton peak for nanowires grown with different V/III ratios. Nanowires grown at the highest V/III ratio of 93 have an exciton lifetime of only 120 ps, significantly shorter than the lifetime of 280 ps for nanowires grown at a low V/III ratio of 11. Clearly, a high V/III ratio decreases the exciton lifetime. This is attributed to the increase in excess As-related defects at high V/III ratios, most likely As antisite defects (As<sub>Ga</sub>). Other possibilities include As interstitials (As<sub>i</sub>), Ga vacancies (V<sub>Ga</sub>) and the EL2 defect. These defects create deep levels which rapidly trap free carriers and act as non-radiative recombination centres, to reduce exciton lifetime.

A high V/III ratio imparts some advantages, namely a decrease in twin defect density and a decrease in intrinsic C doping. On the other hand, a very high V/III ratio can induce severe kinking and tapering, and can decrease the exciton lifetime, which is undesirable for many device applications. Consequently, we consider an intermediate V/III ratio as the optimum.

The effects of V/III ratio have also been extensively examined for InP and InAs nanowires. For InP nanowires, Paiman et al. [57] found that kinking not only occurred for very high V/III ratios, but also for very low V/III ratios. Recently, our group has observed a similar trend for InAs nanowires. Interestingly, Paiman et al. [57] also observed that the kinked InP nanowires grown at low V/III ratios were predominantly ZB, whereas straight [1 1 1]B-oriented nanowires grown at intermediate V/III ratios were predominantly WZ. The properties of ZB and WZ InP nanowires are further discussed in Section 8.1.

#### 5.4. Effects of growth rate

In conventional planar growth of bulk III–V materials, a rapid growth rate produces lower quality material. Interestingly, we observed exactly the opposite effect for GaAs nanowires, as will be detailed below.

Higher growth rates were achieved by increasing both group III and group V flows, while keeping the V/III ratio constant. Fig. 5.8 shows FESEM images of nanowires grown at different growth rates. The nanowires grown at rapid growth rates (higher III flow) are markedly less tapered. Furthermore, there was a significant reduction in twin defects with increasing growth rate [53]. PL measurements revealed that C impurity incorporation decreased with increasing growth rate, and the exciton lifetime was unaffected by growth rate [53].

The above discussion demonstrates how tailoring growth parameters, such as temperature, V/III ratio and growth rate, can significantly improve nanowire properties. Table 5.1 summarises the effects of these growth parameters on GaAs nanowires.

### 5.5. Tailoring multiple growth parameters

MOCVD gives a large parameter space within which it is possible to tune many variables in order to obtain nanowires with desired properties. For instance, choosing an

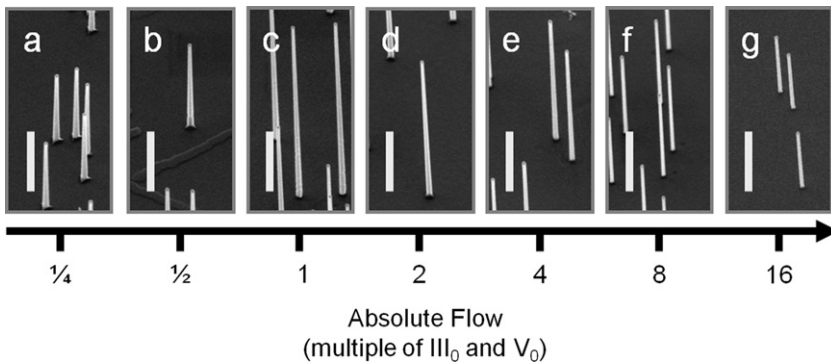


Fig. 5.8. FESEM images of nanowires grown at a constant V/III ratio of 46 and the indicated III and V flows: (a)  $\text{III} = \frac{1}{4}\text{III}_0$  and  $\text{V} = \frac{1}{4}\text{V}_0$ ,  $t = 60$  min, (b)  $\text{III} = \frac{1}{2}\text{III}_0$  and  $\text{V} = \frac{1}{2}\text{V}_0$ ,  $t = 30$  min, (c)  $\text{III} = \text{III}_0$  and  $\text{V} = 1\text{V}_0$ ,  $t = 15$  min, (d)  $\text{III} = 2\text{III}_0$  and  $\text{V} = 2\text{V}_0$ ,  $t = 7.5$  min, (e)  $\text{III} = 4\text{III}_0$  and  $\text{V} = 4\text{V}_0$ ,  $t = 225$  s, (f)  $\text{III} = 8\text{III}_0$  and  $\text{V} = 8\text{V}_0$ ,  $t = 112.5$  s and (g)  $\text{III} = 16\text{III}_0$  and  $\text{V} = 16\text{V}_0$ ,  $t = 56.25$  s. Axis is logarithmic. Samples are tilted at  $40^\circ$ . Scale bars are  $1 \mu\text{m}$ . Reproduced with permission from [53].

Table 5.1

Effects of each growth optimisation on key GaAs nanowire properties: tapering, twin density, intrinsic C doping and exciton lifetime.

Growth optimisation	Improvements in nanowire properties			
	Reduces tapering?	Reduces twin density?	Reduces intrinsic C doping?	Increases exciton lifetime?
Decrease growth temperature	Yes	Yes	Yes	Yes
Increase V/III ratio	No	Yes	Yes	No
Increase growth rate	Yes	Yes	Yes	No

appropriate growth temperature coupled with an appropriate V/III ratio can afford very precise control over nanowire properties. Recently, we succeeded in growing GaAs nanowires with a pure WZ structure, simply by using a high temperature coupled with a low V/III ratio [58]. These nanowires were completely free of stacking faults. Conversely, twin-free zinc-blende nanowires could be obtained simply by using a low temperature coupled with a high V/III ratio, as already discussed in Sections 5.2 and 5.3.

These principles were readily extended to InAs nanowires. Twin-free ZB InAs nanowires were grown using a low temperature and high V/III ratio, whereas stacking fault-free WZ InAs nanowires were grown using a high temperature and low V/III ratio [58].

A final parameter of interest is the nanowire diameter. Paiman et al. [57] observed for InP nanowires that smaller diameters adopt a WZ structure whereas larger diameters adopt a ZB structure. By tailoring both V/III ratio and diameter, Paiman et al. [57] were able to select for either predominantly ZB or predominantly WZ nanowires.

## 6. Ternary and quaternary nanowires

The previous discussion has primarily focused on binary nanowires, composed of only two different elements, such as GaAs. Ternary alloy nanowires, such as InGaAs and AlGaAs nanowires [59], and quaternary nanowires such as InGaAsP, offer further advantages. Their energy bandgap can be tuned by adjusting the composition of the ternary alloy. Ternary and quaternary alloy nanowires enable a greater range of axial and radial heterostructures, and thus broaden the application range of nanowires. For example, the  $\text{In}_x\text{Ga}_{1-x}\text{As}$  material system is of paramount importance in applications such as long wavelength optical transmission and integrated photonics. It is expected to have significant importance in nanowire photonics and electronics.

The development of ternary and quaternary nanowires is complicated by the different growth behaviours of the different elements comprising the nanowire. The different decomposition, diffusion and incorporation efficiencies of the various precursors determine the final nanowire properties, including composition and compositional uniformity. For instance, consider InGaAs nanowires. In adatoms have a significantly larger  $\lambda_s$  than Ga adatoms [60]. Consequently, InGaAs nanowires growing in regions of high nanowire density compete for a limited amount of diffusing In adatoms. InGaAs nanowires in low density regions, however, did not suffer from competition and received a greater flux of diffusing In adatoms. Those nanowires grown in the low density regions had greater axial and radial growth rates and higher In composition than those grown in high density regions. This is clear in Fig. 6.1, where the low density nanowires are significantly taller and have wider bases than the high density nanowires. The PL peak position red-shifted as nanowire density decreased, as shown in Fig. 6.2, indicating that the In content increased with decreasing density. Thus, the InGaAs alloy composition varies across the sample.

The compositional uniformity within each nanowire was also affected. In adatoms have a larger diffusion length and are more readily incorporated into radial growth than Ga adatoms. Consequently, the radial growth is more In-rich. The InGaAs nanowires exhibit In-rich shell, as schematically illustrated in Fig. 6.3. The tapered base of the nanowire is In-rich whereas the tip is Ga-rich.

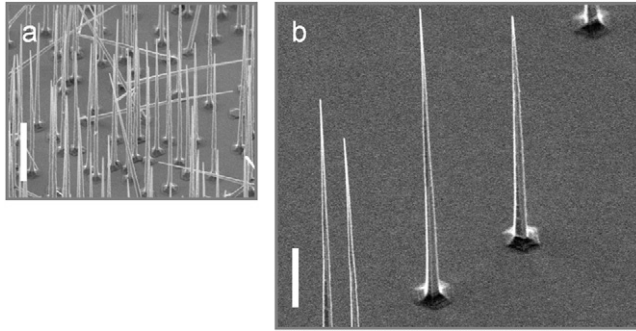


Fig. 6.1. FESEM images of InGaAs nanowires grown at (a) high density and (b) low density. The nanowires of (b) are taller and have wider bases than those of (a). Samples are tilted at  $45^\circ$ . Scale bars are  $2\ \mu\text{m}$ . Reproduced with permission from [60].

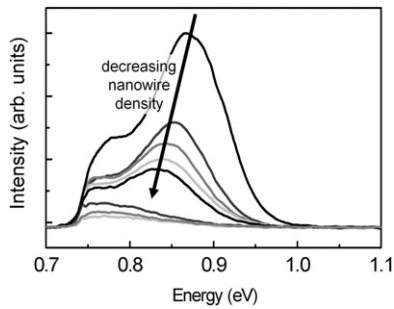


Fig. 6.2. Low temperature (10 K) PL from InAs nanowires in regions of high nanowire density (highest intensity spectrum) decreasing to regions of lower nanowire density (lowest intensity spectrum). The PL peak redshifts with decreasing nanowire density. Reproduced with permission from [60].

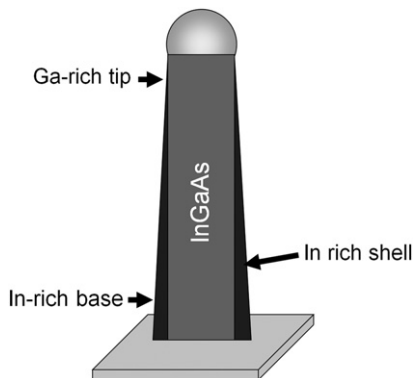


Fig. 6.3. Schematic diagram illustrating the formation of an In-rich shell around an InGaAs nanowire, which results in a Ga-rich tip and an In-rich base.



## 7. Heterostructure nanowires

The cylindrical symmetry of nanowires permits two types of heterostructure: axial and radial.

### 7.1. Axial nanowire heterostructures

Axial nanowire heterostructures are achieved by switching precursor gases during Au nanoparticle-assisted growth, resulting in compositional modulation along the nanowire growth axis. Fig. 7.1 illustrates the growth of an axial heterostructure nanowire. Periodically changing the vapour species produces superlattice nanowires.

In axial heterostructure nanowires, the narrow nanowire diameter allows the nanowire lattice to radially expand or contract, and hence can relieve strain between lattice-mismatched materials without necessitating strain-relieving misfit dislocations [61,62]. This permits high quality heterointerfaces, at which misfit dislocations are seldom observed, within axial heterostructure nanowires of highly lattice-mismatched materials. Thus, nanowires present a major advantage over planar and bulk materials, where lattice mismatch and strain have precluded the growth of high quality coherent heterointerfaces.

Although axial and substrate–nanowire heterostructures are relatively immune to lattice and thermal mismatch effects, there are limitations on these structures. The first limitation we will discuss is imposed by the difference in surface and interface energies of the different materials comprising the heterostructures. Consider Fig. 7.2, in which a material B is grown on top of a material A. There are three important interfaces in this system: the heterointerface between segments A and B (A–B interface), the interface between the growth-directing Au nanoparticle (NP) and material A (NP–A interface), and the interface between the Au nanoparticle and material B (NP–B interface). Their interfacial energies are denoted  $\gamma_{A-B}$ ,  $\gamma_{NP-A}$  and  $\gamma_{NP-B}$ , respectively.

To create the axial A–B heterostructure of Fig. 7.2a, the formation of the new A–B and NP–B interfaces must be thermodynamically favourable. That is, the total interface energy of the two new interfaces is less than or equal to the original interface energy, such that

$$\gamma_{NP-B} + \gamma_{A-B} \leq \gamma_{NP-A}. \quad (1)$$

In this case, layer-by-layer growth occurs, with a B layer forming across the A layer, and a straight nanowire heterostructure will result. If, however, the new total interface energy exceeds that of the original interface,

$$\gamma_{NP-B} + \gamma_{A-B} > \gamma_{NP-A}, \quad (2)$$

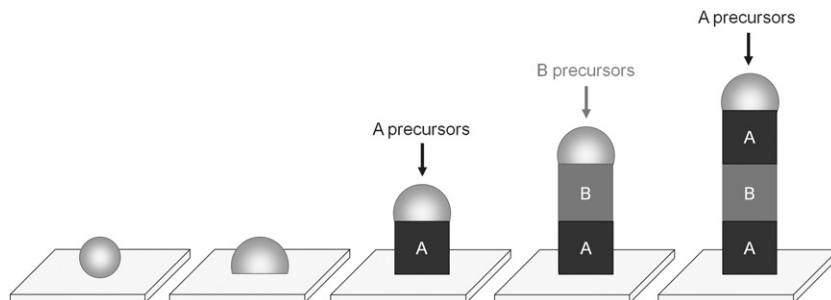


Fig. 7.1. A schematic diagram illustrating the growth process of an axial heterostructure nanowire.

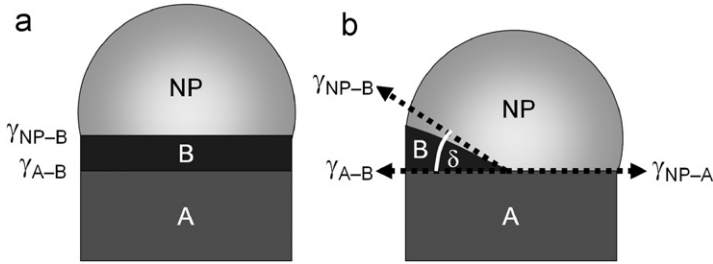


Fig. 7.2. Schematic diagram of the two different growth modes of heterostructure nanowires: (a) layer-by-layer growth and (b) island growth.

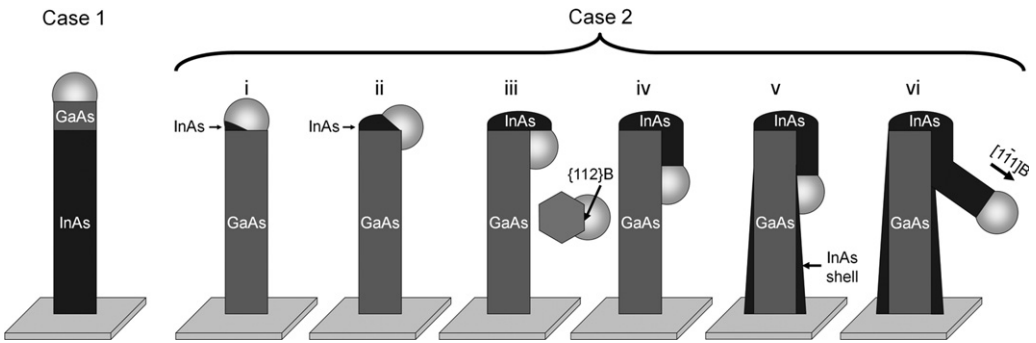


Fig. 7.3. Axial growth schemes. In Case 1, GaAs growth occurs in a layer-by-layer fashion, resulting in an axial GaAs segment on top of the InAs segment. In Case 2, InAs forms an island (i), rather than a continuous layer. The Au nanoparticle migrates to maintain a low energy interface with the original GaAs nanowire (ii–iv). As the Au nanoparticle migrates off the nanowire tip and down the  $\{112\}B$  nanowire sidewall, it catalyses growth of an InAs segment on the sidewall. Concurrently, radial growth produces an InAs shell surrounding the GaAs core (v). When the Au nanoparticle meets the InAs shell, it can no longer maintain an interface with GaAs. The energetically favourable interface changes to an Au nanoparticle–InAs  $[111]B$  interface. Growth proceeds in this  $[111]B$  direction, causing an InAs branch, or kink (vi).

layer-by-layer growth is not energetically favourable. Instead, an island of material B will form (Fig. 7.2b). The island geometry minimises the A–B and NP–B interfacial areas, while retaining the NP–A interface, with its low interfacial energy. This mechanism of island formation is known as the Volmer–Weber growth mode.

We exemplify the phenomenon with GaAs–InAs heterostructures nanowires, as illustrated in Fig. 7.3. In Case 1, the GaAs segment is grown after the InAs segment. In this case, axial growth of GaAs continues in a layer-by-layer fashion in the vertical  $[111]B$  direction. Using Eq. (1), we note that  $\gamma_{NP-GaAs} + \gamma_{GaAs-InAs} \leq \gamma_{NP-InAs}$ . In Case 2, the InAs segment is grown after the GaAs segment. In this case, the InAs forms an island. Using Eq. (2), we note that  $\gamma_{NP-InAs} + \gamma_{GaAs-InAs} > \gamma_{NP-GaAs}$ . Combining the two cases, we find that  $\gamma_{NP-InAs} > \gamma_{NP-GaAs}$ . Thus, the NP–GaAs interface is more energetically favourable than the NP–InAs interface. As a consequence, the Au nanoparticle migrates to retain the energetically favourable Au–GaAs interface, even with continuing InAs growth: the Au nanoparticle slides off the nanowire tip and down the GaAs nanowire sidewall, assisting InAs growth as it migrates.

The Au nanoparticle slides down one of the three  $\{1\ 1\ 2\}$ B sidewalls, which have lower interfacial energy than the three  $\{1\ 1\ 2\}$ A sidewalls [63]. The InAs forms a cap on top of the GaAs nanowires and then grows downward in a  $[1\ 1\ 1]$ A direction [64].

Case 2 is further complicated by the radial growth, as indicated in Fig. 7.3(v) and (vi). InAs radial growth, which occurs concurrently with InAs segment growth, produces an InAs shell around the GaAs segment. With sufficient InAs shell growth, the Au nanoparticle, while sliding down the GaAs sidewall, ultimately meets a continuous InAs shell. At this point, the Au nanoparticle can no longer maintain an interface with the GaAs, and instead contacts the InAs shell. The energetically favourable interface then changes to an Au nanoparticle–InAs  $[1\ 1\ 1]$ B interface. Growth then proceeds in this  $[1\ 1\ 1]$ B direction. The result is a branched, or kinked, heterostructure nanowire, as illustrated in Fig. 7.3(vi) [65].

The second limitation we will discuss is the difficulty in obtaining atomically abrupt interfaces. Some heterostructures form diffuse interfaces, for example, GaAs/InAs heterostructure nanowires, in which a GaAs segment grows on an InAs segment [66]. During growth of the lower InAs segment, the nanoparticle is an Au–In alloy. To grow the upper GaAs segment, the In precursor gas is removed and the Ga precursor gas is introduced. At this point, an Au–In–Ga alloy forms. The nanoparticle thus behaves as a reservoir of In, even after the In precursor gas has been removed. During growth of the nominally GaAs segment, the nanoparticle gradually releases In, which is incorporated into the GaAs segment. Consequently, the GaAs/InAs heterointerface is diffuse [66].

Unlike the diffuse GaAs/InAs heterointerface, the InAs/GaAs interface is atomically abrupt. In these heterostructures, the InAs segment is grown on top of the GaAs segment [66]. To grow the upper InAs segment, the Ga precursor gas is removed and the In precursor gas is introduced. In this case, Ga is rapidly expunged from the nanoparticle under the In vapour. This suggests that In has greater thermodynamic affinity towards the Au nanoparticle than Ga, resulting in a sharp InAs/GaAs interface but a diffuse GaAs/InAs interface [66].

The nature of the interface (diffuse or abrupt) depends on the alloy formed by the Au nanoparticle. Group III elements Ga, In and Al, and the group V element Sb, all alloy with Au. For these elements, the Au alloy nanoparticle can act as a reservoir of the element, even after the element's precursor gas has been removed from the growth chamber. If the heterostructure involves switching one of these elements, a diffuse interface may result, as already discussed for GaAs/InAs heterostructure nanowires. In contrast, group V elements As, P and N do not alloy appreciably with Au. The Au nanoparticle does not act as a reservoir for these elements. If the heterostructure involves switching one of these elements to another, the interface will be abrupt, for instance InAs/InP and GaP/GaAs heterostructures nanowires.

The third limitation is unintentional concurrent radial growth. Consider the growth of a segment of material B on a lower segment of material A (Fig. 7.4). During the axial growth of the upper B segment, some material B may incorporate radially onto the sidewalls of the lower A segment. This radial growth creates a shell of material B around the lower segment of material A. This unintentional shell can adversely affect nanowire device function. Minimising radial growth is therefore important for the development of axial heterostructures.

## 7.2. Radial nanowire heterostructures

Radial heterostructure nanowires are also known as core–shell nanowires. The nanowire core is grown first, by the Au nanoparticle-assisted mechanism. Then the precursor gases are changed and growth conditions are changed to promote radial growth and hinder axial

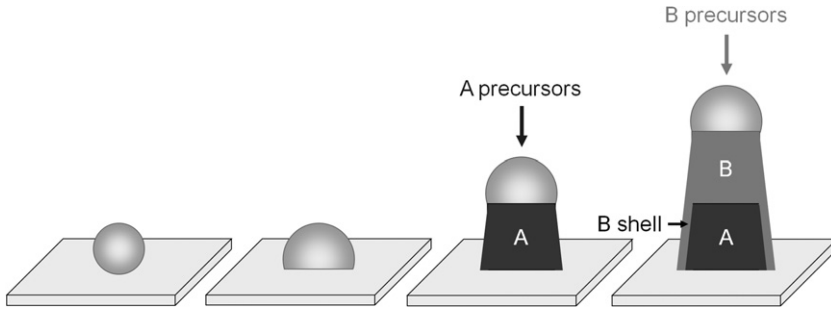


Fig. 7.4. Schematic diagram of how radial growth results in unintentional shell growth around the axial heterostructure nanowire.

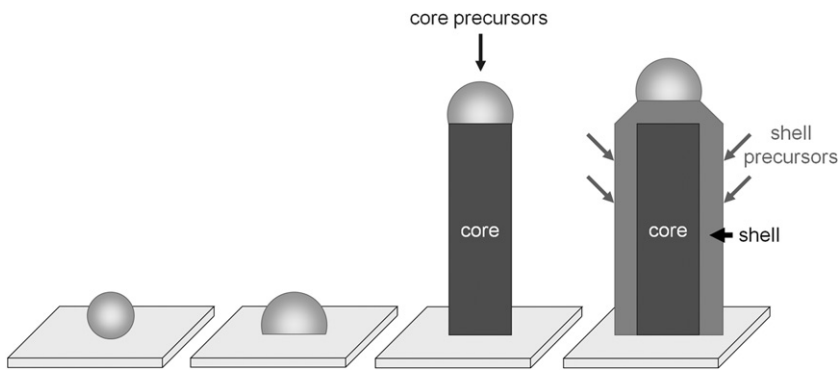


Fig. 7.5. A schematic diagram illustrating the growth process of a radial heterostructure nanowire, with axial core growth followed by radial shell growth.

growth. By this latter step, material is deposited laterally around the nanowire as a shell. This process is illustrated in Fig. 7.5. Multiple shell layers can be deposited, to create core–multishell nanowires.

Typically, core growth is achieved at low growth temperature conducive to axial Au-assisted growth, whereas shell growth is achieved at a higher temperature conducive to radial growth. An example is the growth of GaAs–AlGaAs core–shell nanowires. The GaAs core is grown at low temperatures, for instance 450 °C. The AlGaAs shell is grown by raising the growth temperature to 650 °C. Note that, without the AlGaAs shells, the GaAs cores exhibit only weak PL due to the high density of surface states at which carriers recombine non-radiatively. In GaAs–AlGaAs core–shell nanowires, the wider bandgap AlGaAs shell passivates surface states on the GaAs nanowire core. The AlGaAs coating markedly improves the photoluminescence. Generally, after AlGaAs shell growth, we grow a final GaAs cap, or “skin” layer (also grown at 650 °C). This thin GaAs skin layer protects the underlying AlGaAs shell from oxidation. These heterostructures are known as “core–shell–skin” nanowires. Generally, the AlGaAs shell is approximately 30 nm thick, and the GaAs skin is approximately 5 nm thick.

When the materials are mismatched, core–shell and shell–shell interfaces are prone to misfit dislocations [67]. The lattice of radial heterostructures cannot relax to relieve strain,

unlike axial heterostructures. The crystal structure of the shell tends to follow the crystallographic structure of the core: ZB shells grow on ZB cores (e.g. ZB InAs shells on ZB GaAs cores) [67] and WZ shells grow on WZ cores (e.g. WZ GaAs shells on WZ InAs cores) [68].

Shell growth can lead to a number of interesting phenomena. One example is the asymmetric radial growth of InAs “ribbons” on the three alternate  $\{1\ 1\ 2\}$ A faces of GaAs cores [69]. This occurs because the three  $\{1\ 1\ 2\}$ A faces have a faster growth rate than the  $\{1\ 1\ 2\}$ B faces. The growth of InAs ribbons is schematically illustrated in Fig. 7.6b.

Another example is the radial growth of InAs “rings” when the GaAs core presents concavities [67]. The GaAs core, with concave and convex portions, is illustrated in Fig. 7.6c. Deposition of rings occurs because the chemical potential, which is the thermodynamic driving force for growth, varies along the nonplanar GaAs surface. The chemical potential of a nonplanar surface can be expressed as

$$\mu = \mu_0 + \Omega E_s(x, y) + \Omega \gamma \kappa(x, y)$$

where  $E_s(x, y)$  is the local strain energy at the surface,  $\Omega$  is the atomic volume of the reaction species,  $\kappa(x, y)$  is the surface curvature and  $\gamma$  is the surface energy. Thus, the  $\Omega E_s(x, y)$  term describes the effect of strain and the  $\Omega \gamma \kappa(x, y)$  term describes the effect of surface curvature (or capillarity). During radial InAs deposition, the adatoms migrate to regions of lower chemical potential, and stable nuclei form in these regions. In the initial stages of growth, InAs deposition takes place preferentially at the two convex edges of the concave regions, which effectively relaxes strain and minimises the formation of misfit dislocations. Concave regions present a local decrease in chemical potential due to their surface curvature. Consequently, adatoms diffuse towards these concave areas and incorporate there (Fig. 7.6d). Once the concave regions are filled, further InAs growth takes place on the pre-existing InAs portions. With continuing growth, the three radially distributed InAs regions expand and connect, to form InAs nanorings (Fig. 7.6e) [67].

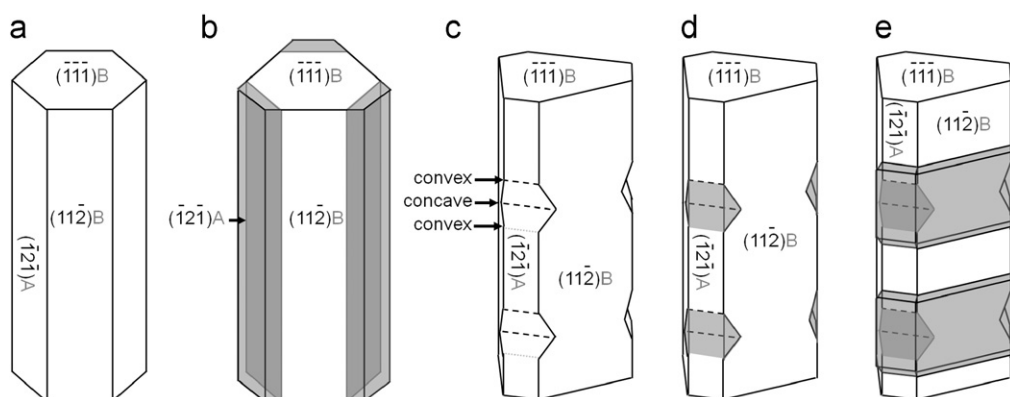


Fig. 7.6. (a) GaAs core with three  $\{1\ 1\ 2\}$ A and three  $\{1\ 1\ 2\}$ B facets. (b) GaAs core of (a) with InAs ribbons grown radially on the  $\{1\ 1\ 2\}$ A facets. (c) GaAs core with concave and convex portions. (d) GaAs core of (c) with InAs sections growing in the concave regions. (e) With further growth of InAs, the InAs sections expand to form an annular shape connecting the three concave regions. Note that polar facets are labelled as “A” or “B” in feint font.

These hierarchical heterostructures, including nanoribbons and nanorings, exhibit novel physical properties, and may be used as future building blocks to extend the applications of semiconductor nanowires.

### 7.3. Nanowire–substrate heterostructures

A further type of heterostructure is the nanowire–substrate heterostructure. As explained for axial heterostructure nanowires, the narrow nanowire diameter permits lateral relaxation of the nanowire lattice. This concept extends to nanowire–substrate heterostructures, where nanowires can be grown epitaxially on a lattice-mismatched substrate without misfit dislocations. This has allowed, for example, the integration of III–V nanowires with existing Si electronics: nanowires can be grown epitaxially on Si substrates, despite the large lattice and thermal mismatch.

As with axial heterostructures, nanowire–substrate heterostructures are also affected by the surface and interface energies of the different nanowire and substrate materials. As discussed in Section 7.1, the Au nanoparticle tends to retain the lower energy interface, which may be the Au nanoparticle–substrate interface. If this is the case, the Au nanoparticle will migrate along the substrate surface, rather than initiating axial  $[1\ 1\ 1]_{\text{B}}$  nanowire growth. A clear example is the Au-assisted growth of InAs nanowires on GaAs  $(1\ 1\ 1)_{\text{B}}$  substrates. In this case, the Au nanoparticle–GaAs interface is more energetically favourable than an Au nanoparticle–InAs interface [70]. For this reason, the Au nanoparticle retains the interface with the GaAs substrate, and minimises its contact with the growing InAs. Consequently, the Au nanoparticle migrates along the GaAs substrate surface, whilst assisting InAs growth as it moves. Thus, an InAs “trace” follows the movement of the Au nanoparticle, as shown in Fig. 7.7. The Au nanoparticle maintains two interfaces: an interface with the GaAs  $(1\ 1\ 1)_{\text{B}}$  substrate, and an interface with a  $\{1\ 1\ 1\}$  plane of the growing InAs. This constrains the traces to elongate along the  $\langle 1\ 1\ 2 \rangle$  directions. Eventually, the migrating nanoparticle intersects with another InAs trace. At this point, the Au nanoparticle can no longer maintain an interface with the GaAs  $(1\ 1\ 1)_{\text{B}}$  substrate. To minimise interfacial energy, a new Au nanoparticle–InAs  $(1\ 1\ 1)_{\text{B}}$  interface forms. This interface is parallel to the substrate plane. Thereafter, InAs deposition occurs

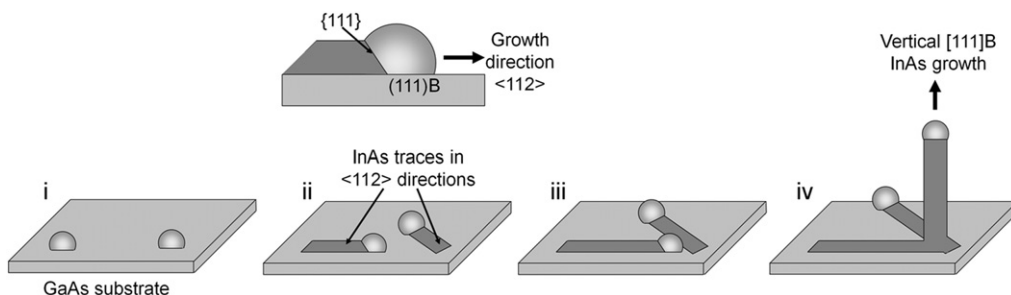


Fig. 7.7. Illustration of the growth progression of InAs traces and nanowires on a GaAs  $(1\ 1\ 1)_{\text{B}}$  substrate. Initially the Au nanoparticle migrates along the GaAs surface to maintain the low energy Au nanoparticle–GaAs  $(1\ 1\ 1)_{\text{B}}$  interface. This produces trace-like growth of InAs in the  $\langle 1\ 1\ 2 \rangle$  directions. When the migrating Au nanoparticle meets another trace, it can no longer maintain an interface with GaAs. It instead forms an InAs  $(1\ 1\ 1)_{\text{B}}$  interface so that Au nanoparticle-assisted axial InAs nanowire growth takes place.

at this Au nanoparticle–InAs (1 1 1)B interface so that vertical [1 1 1]B InAs nanowire growth takes place.

## 8. Photoluminescence spectroscopy of semiconductor nanowires

The optical and electronic properties of semiconductor nanowires and nanowire heterostructures can be probed using the powerful optical characterisation techniques of photoluminescence spectroscopy including continuous wave (CW-PL), resonant, time-resolved and polarisation spectroscopy. These techniques provide insights into the crystalline quality, the energy bandgap (or bandgaps in the case of heterostructures), the excitonic structure, crystalline defects, doping, crystalline phase, and spin and exciton lifetimes—all qualities relevant to particular nanowire device applications. In the sections below, we explore the contributions to our understanding of the III–V nanowires presented in the previous sections. First we discuss CW-PL, then polarisation spectroscopy, resonant spectroscopy, time-resolved spectroscopy and finally Raman spectroscopy. We provide several key experimental details about each technique. In addition, we connect our discussion of the results to the central qualities of nanowires identified via different growth parameters and materials to provide insights into a wide range of physical properties one can determine from spectroscopic techniques, from bandgaps to exciton lifetimes. We pay special attention to the properties of the nanowires that should enable flexible and unique device applications.

Semiconductor nanowires are named appropriately in the sense that their diameters are clearly in the nanometre range, e.g. 20–100 nm, a scale that will be important, but a scale often not in the quantum regime. Since the exciton diameter is 24 nm for GaAs, 18 nm for InP, and 68 nm for InAs, quantum effects only begin to become important for nanowires whose diameters are smaller than 20 nm. While the majority of the nanowires are grown with 20, 30 and 50 nm gold catalysts, once the nanowires have grown 2–10  $\mu\text{m}$  in the axial (lengthwise) direction, they almost always range from 30 to 80 nm in diameter. Thus quantum effects are nearly insignificant for the nanowires considered in this review. In fact, in the previous 10 years of growth, only a single paper on InP nanowires in 2001 [71] and a single paper on GaAs in 2009 [72] showed conclusive evidence for quantum confinement effects.

Nonetheless, dramatic effects on the electronic and optical properties of semiconductor nanowires still occur on the <100 nm diameter length scale, in particular in two areas: for the excitation and emission from these nanowires and in the diffusion of carriers within the nanowires. The relevant optical fields for excitation and emission from these nanowires range in wavelength from 700 to 1600 nm. The nanowire diameters studied here are smaller than these wavelengths by an order of magnitude. As we shall show, this has dramatic consequences on the excitation and emission of electronic states in nanowires. For carrier or exciton diffusion, the low temperature hole mobilities, ranging from 1000 for InP to 10,000  $\text{cm}^2 \text{V}^{-1} \text{s}^{-1}$  for GaAs and recombination lifetimes ( $\sim 1$  ns) suggest diffusion lengths of several microns. This implies that the electrons and holes can sample nearly the entire volume of the nanowire during their lifetime. Thus the quality of surfaces or interfaces of the nanowire and uniformity of dimensions are key elements in the nanowire properties. Even for perfectly crystalline semiconductor nanowires (no defects), the variability of the surface or interfaces of individual nanowires can result in quite dramatic changes in their properties. Measurements of ensembles of nanowires, while informative,



can be misleading since the wire-to-wire variability can be so large as to mask the key physical properties of the individual nanowires. This collective effect is observed in larger linewidths, defect lines at unexpected energies, and inconsistent lifetimes. Therefore, all of the optical measurements described in this section are on single nanowires; however, multiple single nanowires are usually studied to insure generalisability of results.

To carry out our measurements of single nanowires, we remove some of the nanowires from the growth substrate and disperse them onto a silicon substrate in one of the two ways. The first method is to place a small piece of the growth substrate into a methanol solution in a small beaker and sonicate using an ultrasonic cleaner followed by placing a droplet on a Si substrate, and the second method is to mechanically slide a small piece of the growth substrate (nanowires down) across a silicon substrate. In order to identify individual nanowires among the hundreds distributed across the silicon substrate, the silicon substrate is pre-marked with an alignment grid using photolithography, thermal evaporation of an aluminium metal film, followed by lift-off. The  $5 \times 5$  array of L's is spaced  $10 \mu\text{m}$  apart and each array is individually marked (Fig. 8.1). Even though the diameters of nanowires can be much less than  $100 \text{ nm}$ , their lengths (several microns) make them easily visible in a light- or dark-field microscope. Microscope images of various regions of the substrate make it possible to identify 20 or 30 good-length, separate nanowires which are then briefly surveyed individually at low temperatures using power- or polarisation-resolved measurements. Van-der Waals forces hold the nanowires on the substrate, so that they can be found and studied repeatedly over several weeks or even months.

In Section 8.1, we first describe the CW-PL measurements of single nanowires at variable temperatures. In Section 8.2, we discuss the distinctive effects of nanowires on the polarisation of the incoming and outgoing electromagnetic fields. Section 8.4 illustrates the effects of phonon coupling to excitons in nanowires, and evidence for control of excitonic wavefunctions through polarised resonant excitation. Section 8.5 describes the dramatic effect surface and volume defects have on the recombination dynamics and quantum efficiencies in nanowires and methods to optimise their growth so as to minimise them. We also investigate many-body effects of high densities of electrons and holes within nanowires as well as their dynamics. In Section 8.6 we discuss some recent measurements on highly strained core-shell nanowires where both Raman scattering and PL are used to elucidate the physics. Finally, in Section 8.7 we summarise and conclude this discussion of the optical and electronic properties of III-V nanowire heterostructures.

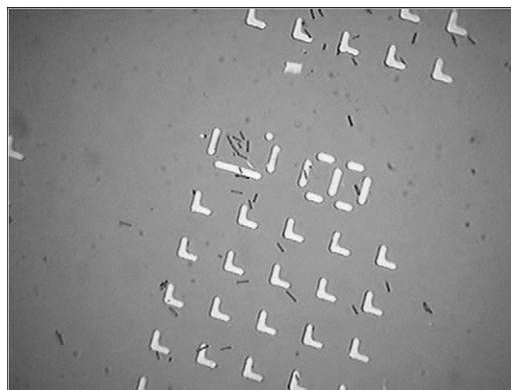


Fig. 8.1. Patterned Si substrate with nanowires deposited for low temperature optical studies.

### 8.1. Photoluminescence emission from nanowires and defects

CW-PL spectroscopy provides fundamental information like the bandgap of the nanowire. CW-PL spectroscopy is carried out on single nanowires distributed on a silicon substrate with markings which allow one to return to the same nanowire for additional measurements. The exciting radiation from a variety of laser sources is focused on an individual nanowire using a  $50 \times / 0.5\text{NA}$  ultra-long working-length microscope objective providing a  $1.2 \mu\text{m}$  excitation spot on the nanowire in the cryostat. The photoluminescence is gathered by the same objective (backscattering geometry), and directed into a spectrometer equipped with a CCD array detector. Polarisation of both the excitation radiation and the emitted photoluminescence is utilised as appropriate.

Both bulk InP and InP nanowires usually grow with cubic crystalline ZB structure. However, the CW-PL spectra as a function of temperature displayed in Fig. 8.2 for two InP nanowire samples, suggest one nanowire has a ZB crystal structure and the other WZ crystal structure, each with a characteristic bandgap [73]. A spectrum from an InP epilayer is also displayed, bottom left of Fig. 8.2. One immediately observes that the bandgap energy, the energy of the recombining excitons displayed as a peak in the spectra, is quite different for the ZB and WZ structures. The WZ InP nanowire has a bandgap 80 meV higher than the ZB InP nanowire. The fact that the temperature dependence of the energy of the emission lines follows the same trajectory, and that the exciton emission quenches at similar temperatures [73], indicates that the phonon frequencies and electron and hole masses must be fairly similar between the two nanowire phases.

Because the electronic states are so sensitive to the quality of the surface or interface states of the nanowire, all emission lines from nanowires at low temperatures are dominated

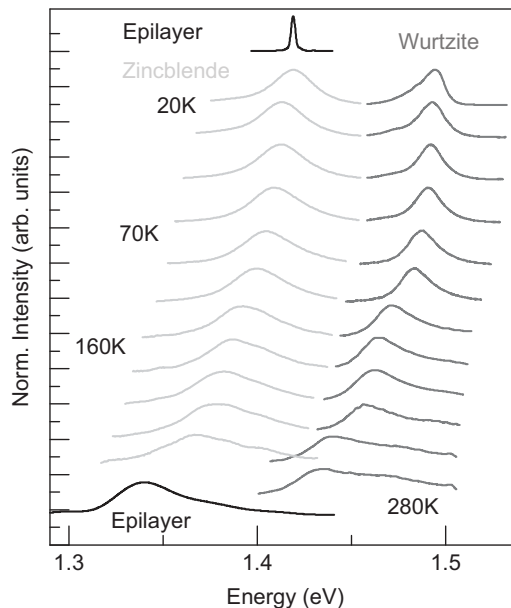


Fig. 8.2. Temperature-dependent CW-PL spectra for a single ZB InP nanowire, a single WZ InP nanowire, and a high quality (1 0 0) InP epilayer. Reproduced with permission from [73].

by significant inhomogeneous broadening. For example, Fig. 8.2 shows a direct comparison between the temperature dependence of a ZB nanowire and a WZ InP nanowire, with a high quality [1 0 0]-oriented InP epilayer grown under optimal conditions. The emission linewidth of the ZB nanowire is over an order of magnitude larger than the emission linewidth of the high quality epilayer. This is typical of nearly every [74] published low temperature spectrum from nanowires, except for excitons localised to a quantum dot embedded within a nanowire [75–77] or excitons localised to morphological defects in CdS nanowires [78]. This means, for example, that it is not possible to identify and distinguish between donor or acceptor bound excitons in these nanowires in order to quantify the dopant density and type directly from PL. However, defect-associated PL from deep levels or donor–acceptor-pair photoluminescence *can be* observed in these III–V nanowires using time-resolved PL spectroscopy as we will discuss in Section 8.5. At higher temperatures, the linewidth is determined by temperature (kinetic) broadening and so the inhomogeneous broadening of the nanowire relative to the epilayer becomes negligible. This means that CW-PL spectroscopy is sensitive only to rather large changes in the energy landscape of a nanowire, such as is observed in the emission from ZB and WZ nanowires as shown in Fig. 8.2. We now investigate how polarisation spectroscopy reveals the crystalline symmetry of single nanowires.

## 8.2. Polarisation spectroscopy of III–V nanowires

As mentioned previously, all of the III–V nanowires studied here have dimensions much larger than the exciton Bohr diameter, so that exciton wavefunctions, masses and binding energies are the same as those observed in epilayers. The optically allowed excitons are spherically symmetric and four-fold degenerate at the centre of the Brillouin zone. Thus one would expect the excitons to emit unpolarised PL after recombination of the electrons and holes. The fact that this is not observed reflects that the nanowire dimensions are much smaller than the wavelength of the incoming and outgoing optical fields which interact with the nanowire. By arranging the polarisation of the excitation laser and the polarisation of the PL admitted to the spectrometer using a Glan–Thomson linear polariser and a Babinet–Soleil compensator and knowing the orientation of the nanowire, we can seek to understand the nanowire’s polarisation response.

We first consider the excitation polarisation of bare GaAs nanowires. The dielectric mismatch between the dielectric of the GaAs nanowire ( $\epsilon \sim 13$ ) and the surrounding air is quite large and can significantly modify the electric field. For an infinitely long cylindrical nanowire of radius  $r$  and with an electric field of wavelength  $\lambda$ , where  $r/\lambda \ll 1$ , the electric field perpendicular to the nanowire is screened:  $E_{\text{int}} = E_{\text{ext}}2/(1+\epsilon)$ . Thus incoming light polarised perpendicular to the nanowire is reduced in intensity by a factor of  $4/(1+\epsilon)^2$  (1/49 for GaAs) when it propagates into the nanowire. Thus light polarised parallel to the nanowire should be nearly 50 times more efficient at excitation of electron–hole pairs than light polarised perpendicular to the nanowire. To measure this effect, Fig. 8.3 (left) shows the integrated intensity emitted from a single GaAs/AlGaAs core–shell nanowire as a function of the linear polarisation angle of the incoming radiation. The GaAs core for this nanowire is 30 nm in diameter and the shell of AlGaAs is 30 nm thick. The emitted PL was analysed for circularly polarised exciton. Fig. 8.3 (right) shows similar data for circularly polarised excitation and linearly polarised emission. One can see that the emitted PL is excited much more efficiently for light polarised parallel to the nanowire rather than

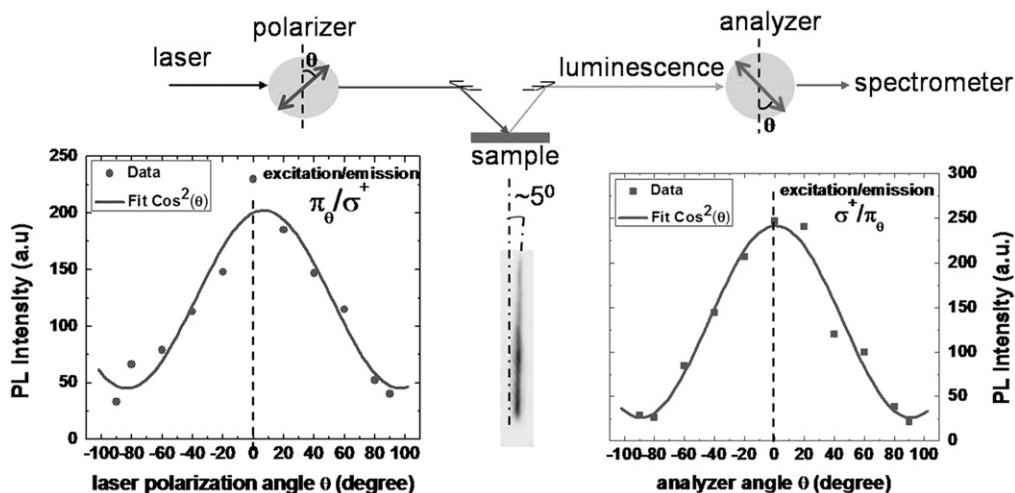


Fig. 8.3. Polarisation-dependent PL measurements of GaAs/AlGaAs core-shell nanowires by varying either the laser excitation orientation with respect to the nanowire (left figure) or the polarisation of the emitted photoluminescence (right figure).

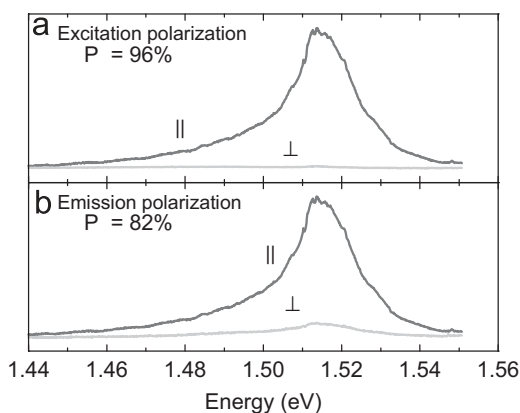


Fig. 8.4. Polarisation dependence of excitation (a) and emission (b) of photoluminescence from GaAs/AlGaAs core-shell nanowires. Reproduced with permission from [79].

perpendicular to the nanowire. Note that this particular nanowire exhibits a maximum 60% polarisation for excitation, rather than the theoretically expected 96%. Fig. 8.4a shows another single nanowire where the observed degree of excitation polarisation is the expected 96%. Thus a significant variation of the degree of polarisation from wire to wire is observed. This degree of variability in polarisation almost certainly reflects the variability of the nanowire symmetry or defects at the nanowire surface. Such behaviour is seen in core-shell as well as bare GaAs NWs.

The PL emitted from the nanowire is strongly polarised as can be seen by the variation displayed in Fig. 8.3 (left) and (right). At first glance this is quite puzzling since even though

excitons with dipoles aligned along the axis of the nanowire are strongly excited by the incoming laser light, they rapidly relax to a random alignment because the two exciton dipole states are degenerate. Excitons with dipoles aligned parallel or perpendicular to the nanowire should be equally probable, resulting in unpolarised light emission as the excitons recombine.

Because the rate at which light is emitted from an exciton population is determined by the radiative lifetime ( $dn/dt = n/\tau_r$ ), the fact that the emitted light is polarised must require that the radiative lifetimes for exciton dipoles aligned parallel to and perpendicular to the nanowire axis be different. In fact, as has been shown by Hoang et al. [80] (see Eq. (2) of Ref. [80]), the radiative lifetimes for exciton dipoles perpendicular to the nanowire are a factor of  $(1+\varepsilon)^2/4$  longer than for excitons aligned parallel to the nanowire axis (a factor of 50 for GaAs). This effect is similar to a reverse Purcell effect where the radiative rate is suppressed as the light field is suppressed. The recombination lifetime of the perpendicular exciton dipoles will be the same as for the parallel excitons, since the much shorter lifetime of these excitons dominates the decay of the exciton population. Just as the excitation polarisation varies from wire to wire, the emission polarisation varies as well.

Since the polarisation effects in semiconductor nanowires reflect their symmetry and uniformity, they can also provide a window into the symmetry of the nanowire crystal structure. We explored this phenomenon for InP nanowires presented earlier (Section 8.1). We observed (see Fig. 8.2) that InP usually appears in nature with the ZB structure, but under certain growth conditions InP nanowires can grow with the hexagonal WZ structure. However, the bandstructure and symmetry of the WZ and ZB semiconductors are dramatically different. Fig. 8.5 shows that the polarisation of the emitted light from ZB and WZ nanowires is indeed distinctively different.

ZB InP nanowires exhibit polarised emission parallel to the nanowire axis because of the dielectric mismatch of the nanowire as described previously. For WZ nanowires, three excitons, A, B, C, may be observed with the A exciton having the lowest energy. The WZ nanowire displayed in Fig. 8.5 is more strongly polarised perpendicular to the nanowire axis than the ZB NW. As discussed by Mishra et al. [73], exciton PL for holes in the lowest energy A band which recombine with electrons in the conduction band is only allowed for the electric field polarised perpendicular to the  $c$ -axis (the growth axis here).

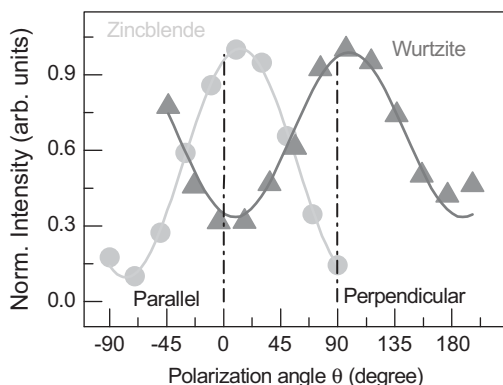


Fig. 8.5. Polarisation dependence of PL emission of ZB and WZ InP nanowires ( $0^\circ$  is parallel to the long axis of the nanowire and  $90^\circ$  is perpendicular). Reproduced with permission from [73].

Because the WZ nanowires grow along the  $c$ -axis of the hexagonal crystal structure, optical transitions should only occur for perpendicular polarisations. The observed polarisation in Fig. 8.5 for the WZ nanowire is clearly less than for the ZB nanowire. This is consistent with the suppression for electric field oriented perpendicular to the nanowire axis. Indeed, recombination is allowed only because of imperfections in the nanowire which is slightly tapered. For a very long, completely symmetric InP WZ nanowire, recombination of the A excitons should be minimal since the electric field is strongly suppressed.

### 8.3. PL spectroscopic mapping of nanowires

A particularly useful way of illuminating PL data for a full nanowire is to create a 2D spectroscopic map as a function of position by collecting a PL spectrum from every point along the nanowire with an optical resolution of  $1.5 \mu\text{m}$ . This can be done in one of the two ways. The first method is to illuminate the entire nanowire at once by defocusing the laser beam, and positioning the nanowire to lie along the entrance slit of the spectrometer. The PL is transmitted through the entrance slit, dispersed by the grating and then imaged onto the entire array of the two-dimensional CCD camera. As displayed in Fig. 8.6 for a

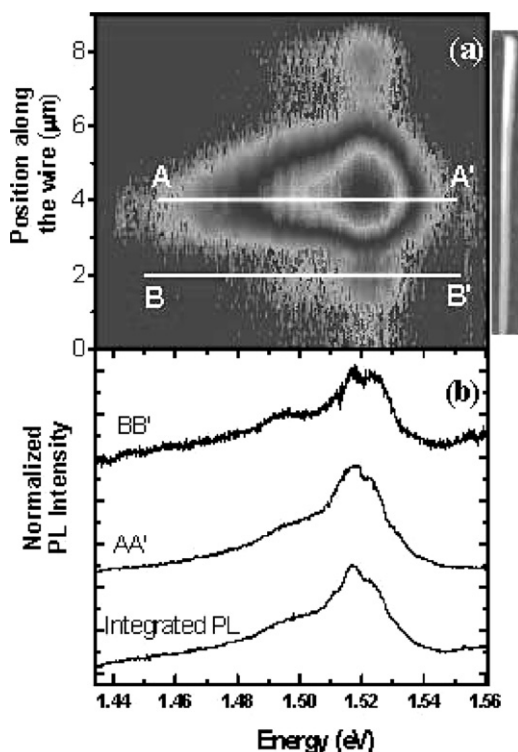


Fig. 8.6. Photoluminescence 2D image at 10 K of (a) energy versus position of a GaAs/AlGaAs core-shell nanowire with PL spectra taken at particular positions along the nanowire length. Two spectra at specific positions (b) along the nanowire. Reproduced with permission from [80].

core-shell GaAs/AlGaAs nanowire, every position along the nanowire image at the entrance slit is mapped to a vertical position along the CCD array. The horizontal position along the CCD array corresponds to the wavelength (energy) of the collected PL. The intensity is displayed in grey scale. Thus in a single exposure the PL spectrum from every position along the nanowire is collected, and stored by the computer as a two-dimensional map.

In Fig. 8.6, the PL intensity is strongly peaked at one position in this GaAs/AlGaAs core-shell nanowire and the analysis power of the 2D map is further demonstrated by the ability to select a single spectrum (see Fig. 8.6b) from any point along the nanowire's length [78]. This is a powerful mapping technique to correlate NW morphology and the observation of spatially resolved PL.

One can also create a 2D map of the polarisation-resolved PL (see also Section 8.2) for the same core-shell nanowire as displayed in Fig. 8.6. We use separate 2D maps of the PL spectra, one for parallel and one for perpendicular emission (Fig. 8.7a and b), to calculate the polarisation defined as  $P = (I_{\parallel} - I_{\perp}) / (I_{\parallel} + I_{\perp})$  along the nanowire (Fig. 8.7c). Fig. 8.7c shows that the emission is strongly polarised along the full length of the nanowire. Data within the white box of Fig. 8.7c is used to generate the histogram of Fig. 8.7d where a maximum polarisation is  $\sim 80\%$ . We will use this data for additional insight into the spin distributions in the next section.

Finally, a spatially resolved photoluminescence excitation (PLE) measurement can be obtained by storing a spatially and spectrally resolved map for every excitation wavelength of the laser as it is tuned to higher energies. In this way the emitted PL and the PLE scan can be obtained for every point along the nanowire.

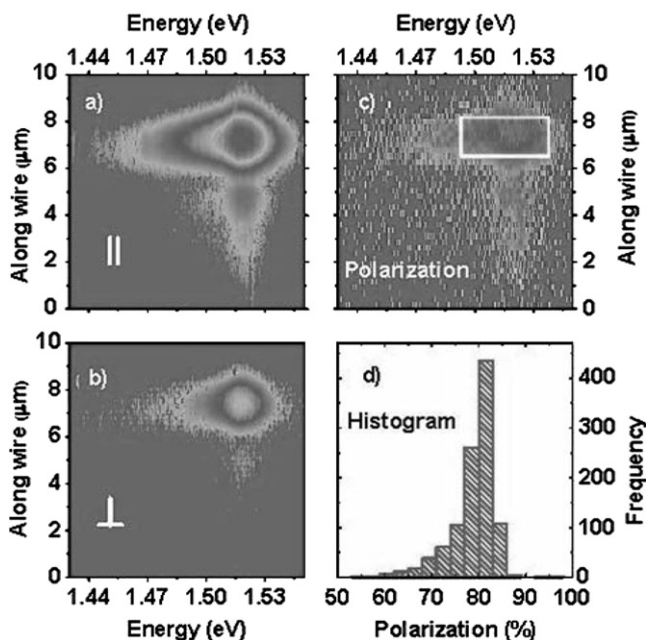


Fig. 8.7. 2D map of polarisation-resolved PL at 10 K for (a) parallel polarised emission, (b) perpendicularly polarised emission, (c) 2D polarisation map, and (d) histogram of polarisation from data within box in (c). Reproduced with permission from [80].



#### 8.4. Resonant spectroscopy of III–V nanowires

Absorption measurements in single nanowires are essentially impossible considering the submicron diameter of the nanowire. Photoluminescence excitation (PLE) measurements, however, can provide equivalent data since one measures the PL intensity of a particular emission line as a function of the laser excitation energy. If an electronic state is excited which is directly coupled to the emission line being monitored, an increase in the emitted PL is observed. For example, Hoang et al. [80] performed a PLE measurement on several single GaAs/AlGaAs core–shell nanowires. Because of momentum conservation, only excitons with momentum very close to zero can recombine, but as the laser energy increases, higher momentum states are excited. The excitons are created with quite high energies which must relax through the emission of optic or acoustic phonons until they can recombine, emitting a photon. If multiple phonon emissions are required to relax the hot excitons, then the longer the relaxation takes, thus increasing the probability that the excitons will recombine non-radiatively. However, when a specific energy is excited which can relax to the very bottom of the exciton band through direct emission of optic phonons, then the excitons relax extremely rapidly to the bottom of the band where they recombine. We see in Fig. 8.8 that strong resonances are observed at 36 and 72 meV above the ground state emission peak at 1.51 eV. These energies correspond to the emission of exactly one or two longitudinal optic phonons in sequence for GaAs. A third peak is observed at 135 meV above the emission peak, which does not correspond to any combination of phonons energies for GaAs. This peak may correspond to excitations directly into the AlGaAs shell.

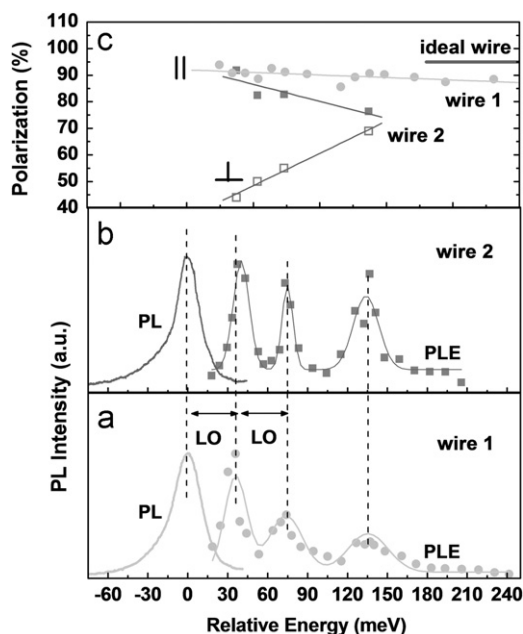


Fig. 8.8. Photoluminescence (solid line) and photoluminescence excitation spectra (solid line with solid circles or squares) for two different GaAs/AlGaAs nanowires (a,b). (c) Polarisation of the photoluminescence as a function of excitation laser energy. Reproduced with permission from [80].

The 135 meV energy corresponds to an aluminium concentration of  $\sim 13\%$ , only half the 26% AlGaAs concentration expected from growth, suggesting that growth of the shell may be limited by diffusion of the constituent atoms along the substrate surface, as was seen previously in InGaAs nanowires by Kim et al. [60].

Resonant spectroscopy also provides insight into the behaviour of spins in these systems. As one excites higher and higher into the exciton band, the excitons must relax through more and more scatterings in order to relax to the bottom of the band. If the excitation laser is polarised parallel or perpendicular to the nanowire, the exciton is created with its dipole oriented either parallel or perpendicular to the nanowire as well. In Fig. 8.8, we monitor the polarisation of the emitted light as a function of the excitation energy. Not surprisingly, at high energies for wire 2, the emitted polarisation is the same regardless of the orientation of the laser. This makes sense because the exciton dipoles will randomise through these scattering processes. What is very interesting is that as the laser energy is reduced, this symmetry is now broken. For parallel excitation, the emission PL is more strongly polarised parallel to the nanowire. For perpendicular excitation the emission PL becomes less strongly polarised. This is consistent with the formation of nonthermal distributions of excitons with more parallel dipoles for parallel laser excitation, and more perpendicular dipoles for perpendicular excitation. Converting parallel dipoles to perpendicular and vice versa requires a spin-flip process, so measuring the relaxation of parallel to perpendicular excitons with laser excitation energy directly measures the spin relaxation time in these nanowires. Through rate-equation analysis solved in steady state (these are CW measurements), we find that the spin relaxation time increases by an order of magnitude as the laser energy comes closer and closer to resonance with the emission line. We estimate that the spin relaxation time is at most 50 ps for resonant excitation [80].

### 8.5. Time-resolved photoluminescence spectroscopy

Time-resolved photoluminescence (TRPL) spectroscopy provides insights into the dynamics of the excitons in nanowires. These measurements are important both for exploring basic science, and for assessing the suitability of nanowires for active device structures. After brief comments on the experimental aspects of TRPL, we provide three examples that illustrate the power of the technique, one of GaAs nanowires, one of InP nanowires, and finally one involving defects in GaAs nanowires.

Time-resolved PL measurements are obtained by focusing the pulsed laser to a particular point on the nanowire, collecting and dispersing the emitted PL in a spectrometer and detecting the emitted photons by either a fast micro-channel plate phototube (MCPT) or a silicon APD with a  $100 \mu\text{m}^2$  active area. Time-correlated photon counting is used [81,82] to accumulate a statistical histogram of the number of photons collected as a function of arrival time after excitation by the laser pulse in order to show the decay of the PL. The system response in our case is less than 80 ps. Full time-resolved spectra are collected by accumulating time-decays as a function of the wavelength of the spectrometer. This allows one to construct a 2D plot of intensity vs. energy and time.

Very recently we have obtained TRPL results from the twin-free GaAs/AlGaAs core-shell nanowire heterostructures. The twin-free GaAs cores were grown by the two-temperature procedure discussed in Section 5.2. These core-shell nanowires were capped by an  $\sim 5$  nm layer of GaAs to prevent oxidation of the AlGaAs which is a potential source of oxygen defects in the core. Earlier TRPL results of GaAs/AlGaAs core-shell nanowires

had suggested exciton lifetimes were below our measurement limit of 80 ps [80]. As shown in Fig. 8.9, we observe for three of these twin-free nanowires, exciton lifetimes of 0.2, 0.6, and 1.1 ns [56]. More than half of the nanowires in this group exhibited long lifetimes of  $\sim 1$  ns, comparable to very high quality MBE-grown double heterostructures. This bodes well for devices requiring long exciton lifetimes including optical devices.

The dynamics of excitons and electron–hole plasmas have been studied both for twin-free GaAs nanowires [56] and InP nanowires [83]. When one uses focused pulsed excitation, one can achieve high electron–hole carrier densities. The dynamics of these can be displayed as a 2D map which displays the evolution of the PL as a function of time. Such a map for an InP nanowire is shown in Fig. 8.10 where the log of the spectral intensities is plotted over an energy range of 1.35–1.50 eV with time evolution from 0 to 3.5 ns. In Fig. 8.10 (upper panel), one can clearly observe that the bandgap and the width in energy of the spectra evolve with time. Slices taken at times indicated by the arrows provide snapshots of the PL (see Fig. 8.10 (lower panel)). At early times, the width and position of the spectra show state filling and bandgap renormalisation which provide information on the carrier density. At later times, excitons appear with a lifetime of 1.1 ns, a lifetime very similar to that observed from the twin-free GaAs/AlGaAs core–shell nanowires above. In this present case, however, the InP nanowires are not heterostructures but simply bare InP nanowires, but benefit from a low surface recombination velocity and thus a relative insensitivity to surface defects.

As another example, we consider defect-associated PL from deep levels or donor–acceptor pair (DAP) photoluminescence in III–V nanowires. For example, in time-resolved spectra from GaAs nanowires in which carbon acceptors have been unintentionally incorporated, a significant DAP PL can be identified because (1) the DAP PL peak saturates with power, while the band edge PL does not, (2) the recombination lifetime of the DAP PL peak is much longer than the band edge PL, and (3) time-resolved spectra show the distinctive movement of the DAP peak to lower energy with time, as can be seen in Fig. 8.11 [52].

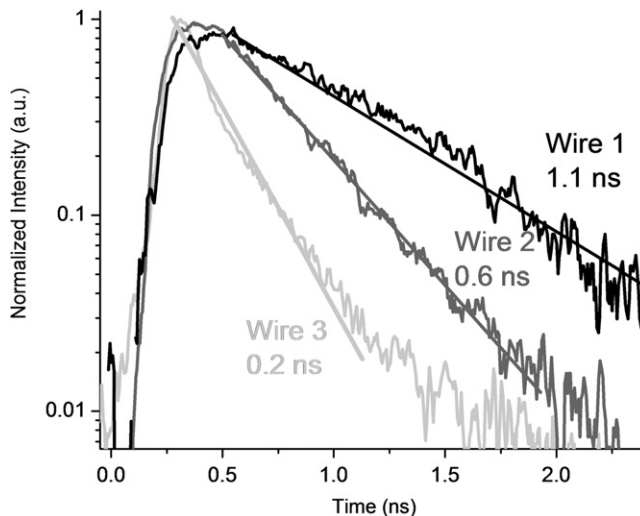


Fig. 8.9. Time-resolved photoluminescence of several twin-free GaAs/AlGaAs core–shell nanowires. Reproduced with permission from [56].

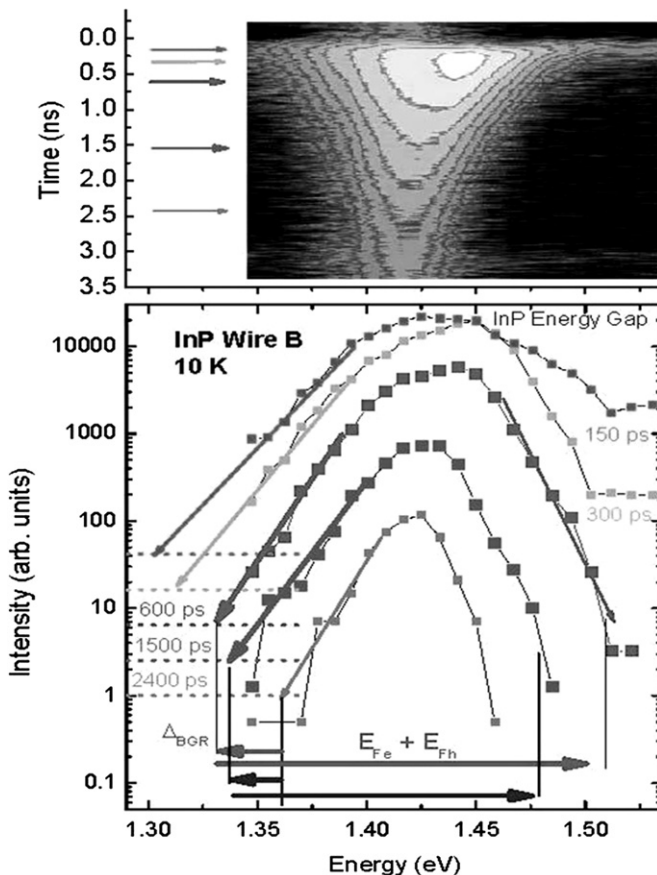


Fig. 8.10. Map of time-resolved photoluminescence spectrum (upper panel) and five slices in the time evolution of the photoluminescence spectrum (lower panel) for an InP nanowire. Reproduced with permission from [83].

In certain cases, spatial imaging of defects can be an important technique in the characterisation of nanowires, particularly if the nanowire defects result from morphological irregularities as was seen in CdS nanowires, or if the number of defects varies during the growth of the nanowires.

### 8.6. Raman characterisation

As a last example, one that takes advantage of both the techniques of Raman scattering and PL spectroscopy, we consider core/shell nanowires composed of two quite disparate materials, namely GaAs (core) and GaP (shell). The lattice mismatch between GaAs and GaP is quite large, 3.6%, and one might reasonably expect the resultant material would be full of defects and dislocations since in 2D epilayers the critical thickness of GaP on GaAs is only 5 monolayers. For GaAs/GaP nanowires, however, we find high optical and structural quality. The lattice mismatch results in significant strain which modifies both the phonon response as well as the electronic structure [84]. Raman scattering from optical phonons was used to obtain both the amount of compressive and shear strain of the GaAs core.

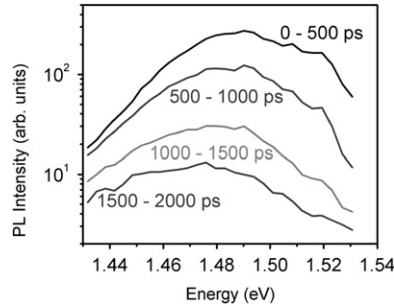


Fig. 8.11. Time-resolved PL measurements from a single GaAs/AlGaAs core-shell nanowire. PL spectra were recorded at consecutive 500 ps intervals after the excitation laser pulse. Reproduced with permission from [52].

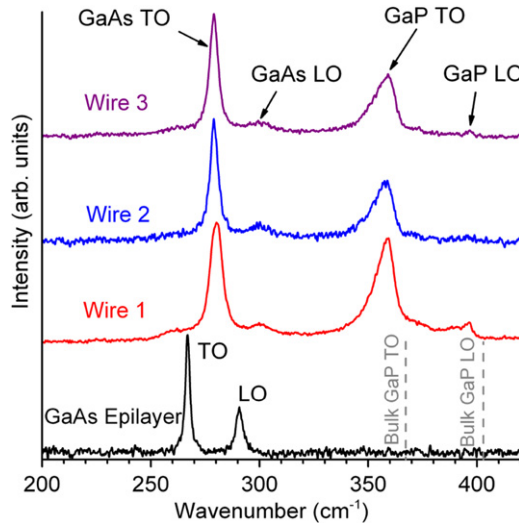


Fig. 8.12. Raman spectra of GaAs/GaP nanowires (upper three traces) and GaAs epilayer (lowest trace) at room temperature. The dashed lines show TO and LO phonon energies of GaP. Reproduced with permission from [84].

In Fig. 8.12, we observe a dramatic increase in the frequency of the nanowire GaAs core TO phonons. Comparing this data with the GaAs epilayer data provides the information needed to extract the compressive and shear strain of the GaAs core caused by the outer GaP shell.

In addition, one can also see that the TO phonon frequency of the GaP shell is significantly downshifted consistent with tensile strain of the shell caused by the core. Once that information is available, one can predict how the electronic structure should be modified. In Fig. 8.13 we see a comparison of the low temperature PL spectrum of an unstrained GaAs/AlGaAs nanowire (recall the lattice constants of the core and shell are very nearly matched in this case) and a strained GaAs/GaP nanowire with a 50 nm diameter core and a 25 nm thick GaP shell. A dramatic change is clearly observed in the PL; the free exciton emission energy increases by  $\sim 250$  meV. The hydrostatic and shear strain obtained from the Raman results predicts the light and heavy hole exciton emission energies indicated by the vertical arrows; the predictions are in good agreement with our PL measurements of the heavy hole exciton. These results – relating strain as measured directly from Raman scattering to the

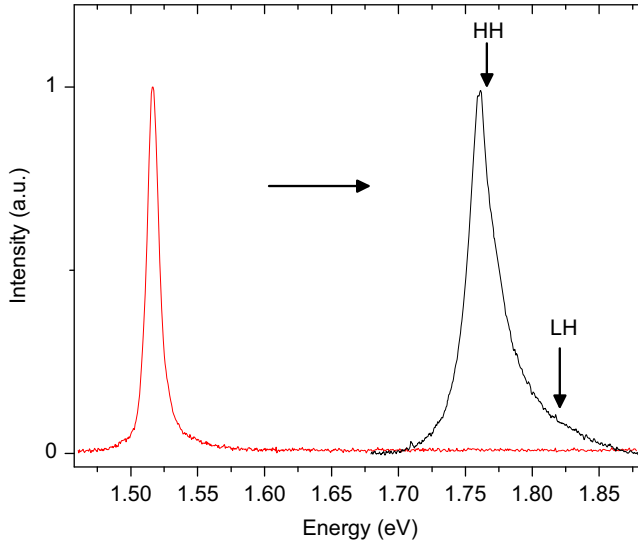


Fig. 8.13. Low temperature PL spectrum of GaAs/AlGaAs nanowire (red peak, left) and GaAs core of GaAs/GaP wire 3 (black curve, right). The emission line shifted  $\sim 260$  meV to higher energy as a result of shell-induced strain. The vertical arrows show energies of HH and LH bandgap, respectively, predicted from Raman measurement. Reproduced with permission from [84]. (For interpretation of the references to colour in this figure legend, the reader is referred to the web version of this article.)

electronic structure obtained from PL measurements – suggest that controlling the strain in core–shell nanowires by varying the nanowire core/shell thickness ratios provides a powerful way to tailor the electronic properties of nanowires for potential applications.

### 8.7. Summary

We have illustrated with specific examples the power of optical photoluminescence to probe the intrinsic and extrinsic properties of semiconductor nanowires. Photoluminescence provides insights into the fundamental bandgap or defect states, while polarisation-resolved PL probes spin states in these systems. Time-resolved PL utilised to measure exciton lifetimes has guided growth parameters and allowed core–shell nanowires with lifetimes nearly that of epitaxial layers to be grown. Combining PL with Raman measurements has opened new possibilities for understanding core–shell nanowires with quite different lattice constants, and thus provided the opportunity to harness strain to tune the properties of these nanowires over a wide range.

## 9. Terahertz conductivity of semiconductor nanowires

Terahertz conductivity spectroscopy (TCS) is a relatively new technique for analysing the electronic properties of materials. This quantitative technique provides a non-contact method of measuring the high-frequency AC conductivity of materials. TCS is particularly well suited to the study of semiconductor nanostructures, owing to the difficulty and artefacts associated with forming direct electrical contacts to nanoscale samples. The photoluminescence techniques described in the previous section provide excellent methods

of characterising semiconductor nanowires. However in order to study the electronic properties of materials with these techniques charge carriers in the samples must be photoexcited and relax via a path involving a reasonably strong radiative transition. For example, the photoluminescence of bare GaAs nanowires is heavily quenched by non-radiative transitions, hence these samples cannot be analysed easily by photoluminescence spectroscopy [79]. TCS measures the dielectric response of a material, and hence does not require the material to emit light, or even be photoexcited.

The simplest form of TCS measures the dielectric response of a material by probing it with a single-cycle electromagnetic pulse of approximately 1 ps duration (this transient is often called a “terahertz” pulse, owing to its peak frequency components being in the THz region when Fourier transformed). In this form of TCS, the sample does not need to be photoexcited. A typical spectrometer can measure the complex conductivity of a material over a frequency range from  $\sim 0.1$  to  $\sim 3$  THz. The spectrometer does not just provide calibrated values of the conductivity; the frequency dependence of the conductivity spectrum also provides a wealth of information about the mechanisms of charge transport in the material.

TCS may also be used to study how the dielectric properties of a material change as a function of time after photoexcitation. In this form of the technique a laser pulse is used to photoexcite the sample and a picosecond electromagnetic “terahertz” pulse is used to analyse the conductivity spectrum at set times after the photoexcitation event. In this way it is possible to observe (i) the portion of the sample’s conductivity that occurs just as a result of photogenerated charge carriers and (ii) how the charge dynamics change on a timescale from  $\sim 100$  fs to  $> 1$  ns after photoexcitation.

It is informative to consider why it is useful to analyse complex conductivity of nanowires at terahertz frequencies ( $\nu \sim 0.1$ – $3$  THz). The best way to put this into context is to consider the energy carried by photon of this frequency range ( $h\nu \sim 0.4$ – $13$  meV). For inorganic semiconductors this is an energy range of collective excitations such as plasmons, excitons and phonons. Thus the occurrence and properties of any of these collective excitations in a sample may be clearly identified by the presence of their signature in the terahertz conductivity spectrum [85,86]. For example, if a semiconductor exhibits a classic Drude-type conductivity of a “free” electron gas then TCS measurements would reveal a spectrum similar to that shown in Fig. 9.1a. In contrast, if the charge carriers were bound as excitons, a Lorentzian conductivity spectrum would result, as shown in Fig. 9.1b. It is also important to note that the 0.4–13 meV-range covered by TCS is non-resonant with electronic transitions, which occur at much higher energies in semiconductors. Thus, TCS spectra are not obscured by strong near-bandgap transitions. Finally, knowing the dielectric response of nanowire at terahertz frequencies will be essential for the exciting and real prospect of integrating of nanowires into ultra-high-speed electronic circuits.

### 9.1. Photoconductivity of GaAs nanowires

In contrast to the PL measurements described in the previous section, all TCS measurements described in this review were performed on an ensemble of GaAs nanowires [87]. In order to obtain well-isolated nanowires they were either grown directly on z-cut quartz substrates, or grown on GaAs substrates and then transferred to a quartz substrate by rubbing. Quartz was chosen as a substrate as it has a negligible dielectric response at



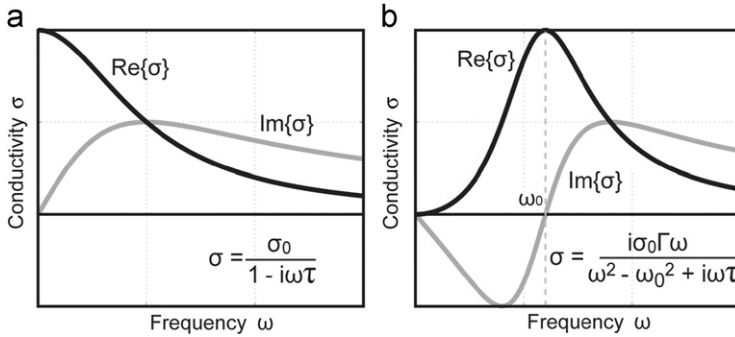


Fig. 9.1. Plots illustrating how information in the spectral conductivity reveals the nature of the charge dynamics: (a) Drude-like free-carriers and (b) Lorentzian type resonance.

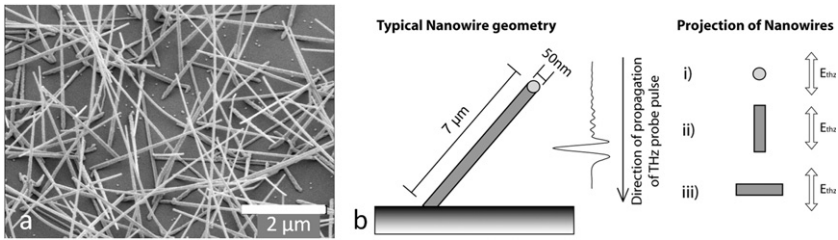


Fig. 9.2. (a) An SEM micrograph shows the typical dimensions and distribution of GaAs nanowires grown on z-cut quartz (scale bar represents 2 μm, image at 45° to substrate normal). (b) A schematic representation of a nanowire, showing the three primary orientations with respect to the terahertz probe: (i) end on, (ii) parallel and (iii) perpendicular.

terahertz frequencies. An SEM of a sample of GaAs nanowires grown on a quartz substrate is presented in Fig. 9.2a. As quartz cannot seed the growth of GaAs, the nanowire axes are distributed over a range of polar and azimuthal angles. The terahertz conductivity of a nanowire depends strongly on the orientation of the nanowire with respect to the direction of the electric field of the terahertz transient,  $E_{\text{THz}}$ . Fig. 9.2b is a schematic diagram of a typical nanowire; case (ii) in the diagram represents the case where  $E_{\text{THz}}$  is parallel to the axis of the nanowire. In this instance one would expect that the conductivity would be close to that of a bulk crystal. However, in cases (i) and (iii) the nanoscale nature of the nanowire is likely to be much more important. Therefore any TCS measurements on such a randomly oriented ensemble of nanowires are likely to produce a superposition of conductivity spectra.

An example of a set of TCS photoconductivity data acquired from an ensemble of nanowires is illustrated by the circles in Fig. 9.3. The TCS data consist of a conductivity spectrum at particular delay times after photoexcitation. In this case the spectra at 50, 350, 500, 650 and 1200 fs after photoexcitation are shown. By analysing each spectrum we obtain a “snap-shot” of the charge dynamics at a particular time after photoexcitation.

A measurement of conductivity  $\sigma(\omega, t) = en(t)\mu(\omega, t)$  does not in itself allow an independent determination of mobility,  $\mu$ , and carrier density,  $n$ . However, these important parameters can be separated by appropriately modelling the frequency dependence of the complex conductivity spectrum. Hence the fact that TCS allows us to measure the fully

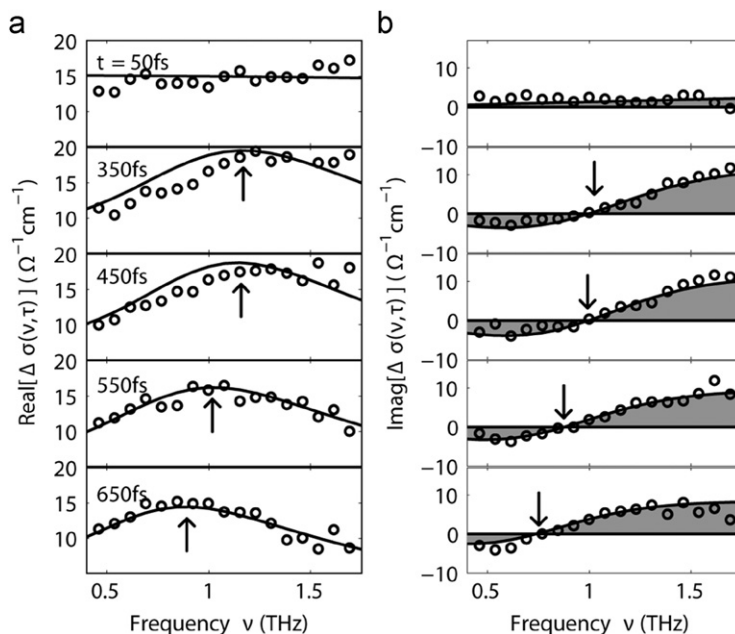


Fig. 9.3. The (a) real and (b) imaginary components of the complex conductivity are shown as a function of frequency, for several delays after photoexcitation (top to bottom). The raw data (circles) are fit with a model based on a superposition of a plasmonic and Drude-type response (lines and filled area), as described in the text. Reproduced with permission from [87].

frequency-dependent complex conductivity of a sample makes the technique particularly powerful.

The data in Fig. 9.3 were modelled using the superposition of a Drude model, and a localised surface plasmon model [85,88], as described in detail in [87]. The Drude model described the population of nanowires with axes aligned with  $E_{\text{THz}}$  (case (ii) in Fig. 9.2b), while the surface plasmon model accounted for the distribution with axis perpendicular to  $E_{\text{THz}}$  (case (iii) in Fig. 9.2b). The population of nanowires with axes parallel to the wavevector of the THz pulse (case (i) in Fig. 9.2b) was ignored owing to their small cross-section. The modelling of the conductivity data is represented by the solid lines in Fig. 9.3.

The key parameters obtained as a result of this modelling are shown in Fig. 9.4 as a function of time after photoexcitation of the nanowires. The squares in Fig. 9.4a represent the density of photoinjected electrons in the nanowires. The electron density decays exponentially with a time constant of 270 fs [87]. This is remarkably short considering a bulk crystal of GaAs typically has a photocarrier lifetime of  $\sim 3.5$  ns for electrons in the vicinity of the surface of the sample and of  $\sim 15$  ns for electrons that have diffused deeper into the crystal [89]. Short carrier lifetimes are important for high speed electronic and optoelectronic components. However, ideal materials for high-speed electronic devices should have a high charge-carrier mobility in addition to a short carrier lifetime [90]. The shaded region in the figure represents the contribution of electron density that is associated with plasmons. These results clearly show that it takes a period of  $\sim 300$  fs for the plasmon mode to become established in the nanowires. This timescale is approximately the inverse of the plasmon frequency.

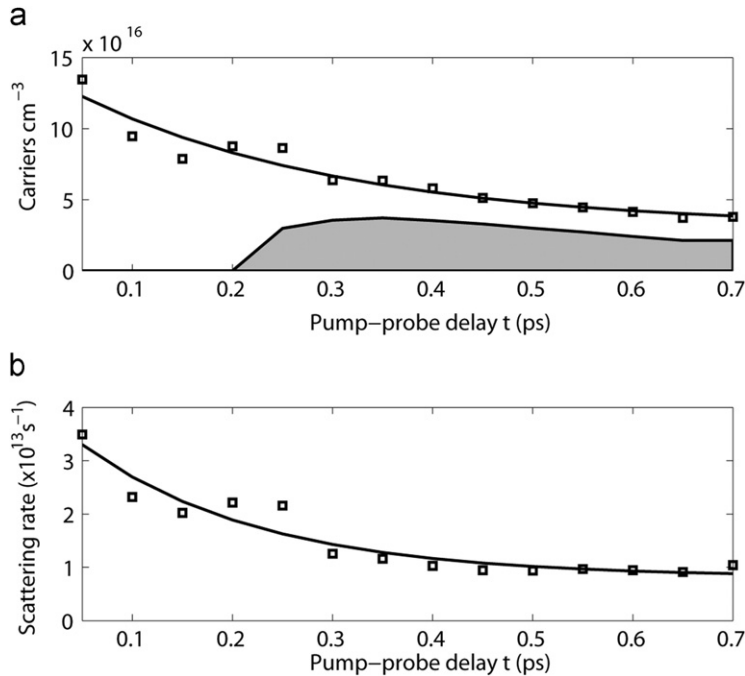


Fig. 9.4. The (a) carrier density and (b) scattering rate are shown as a function of time after photoexcitation. These values are extracted from the frequency domain fits to the photoconductivity (as shown in Fig. 9.3), and provide both the plasmonic and total carrier densities (filled area and squares, respectively). All solid lines are monoexponential fits. Reproduced with permission from [87].

The other key parameter is the electron momentum scattering rate, which is displayed in Fig. 9.4b. It is closely related to the mobility of electrons in the nanowires. The scattering rate also decays exponentially with a time constant of approximately 180 fs.

Thus we conclude that the short (270 fs) carrier lifetime and high mobility of electrons in GaAs nanowires originates from the necessarily high surface-area-to-volume ratio of nanowires. The defects and impurities that are present at a semiconductor–air interface provide sites for charge-carrier trapping. Thus electrons in the vicinity of the surface of a nanowire are quickly trapped. Considering the mean-free-path of electrons in GaAs at room temperature is 44 nm and the diameter of our nanowires is typically 50 nm, the mobility is only weakly degraded from that of the bulk as a typical electron will undergo multiple collisions (momentum scattering events) before interacting with the surface. However the electron will have access to the trapping sites after several collisions, which leads to the short carrier lifetime. The importance for these surface effects has been confirmed by TCS measurements of nanoporous InP, which in many ways are the inverse of nanowires [91,92].

## 9.2. The influence of surface trapping

The photoconductivity analysis described in the previous section also provides an excellent way of analysing charge trapping in nanowires. By photoinjecting increasingly larger densities of electron–hole pairs into nanowires it is possible to begin saturating

trapping centres. By observing this saturation via TCS it is possible to establish the density of traps and the trapping cross-section. These are particularly useful parameters for assessing the purity and quality of nanowires.

Fig. 9.5a shows the (frequency averaged) photoconductivity of an ensemble of GaAs nanowires as a function of time after photoexcitation. In this series of experiments the lowest density of charge carriers (lower trace) was provided by 800 nm-wavelength photons at a fluence of  $0.05 \text{ mJ cm}^{-2}$ , whereas the highest (upper trace) corresponds to a fluence of  $0.84 \text{ mJ cm}^{-2}$ . It can be seen that as the photon fluence is increased the conductivity of the sample becomes higher and remains higher for longer periods after photoexcitation. These data were fitted by a single exponential for delay times between 800 fs and 2 ps. As changes in the scattering rate are insignificant at delay times  $> 800 \text{ fs}$  (see Fig. 9.4b), the decay in conductivity can be directly related to the density of photoexcited electrons,  $n$ , in the nanowire sample. The fitted decay time-constants are plotted as a function of fluence in Fig. 9.5b. The charge carrier density in the nanowires decays much more slowly as the injected carrier density is increased; a 30-fold increase in the injection fluence leads to a doubling in the decay time of electrons.

We have attributed the increase of decay time with photon fluence to a saturation of traps. By modelling our data using a numerical solution of a rate equation for carrier trapping [93] we found the trap density in our GaAs nanowires to be  $2 \times 10^{17} \text{ cm}^{-3}$  and the trapping cross-section to be  $6 \times 10^{-14} \text{ cm}^2$  [87]. As discussed above, owing to the large surface-area-to-volume ratio of nanowires, it is likely that surface states are the primary trapping sites.

In general, while the high surface trap density leads to a short carrier lifetime which is beneficial for fast optical switching, the implementation of nanowires for the full range of nanoelectronic applications requires a method of controlling the carrier lifetime. Typically, defect states may be removed from the GaAs surface using a chemical passivation technique [94] which has previously been shown to lead to an order of magnitude reduction in surface trap density [89]. The bottom-up growth technique of MOCVD also allows the surface to be “overcoated” with a higher bandgap material before the nanowire is exposed

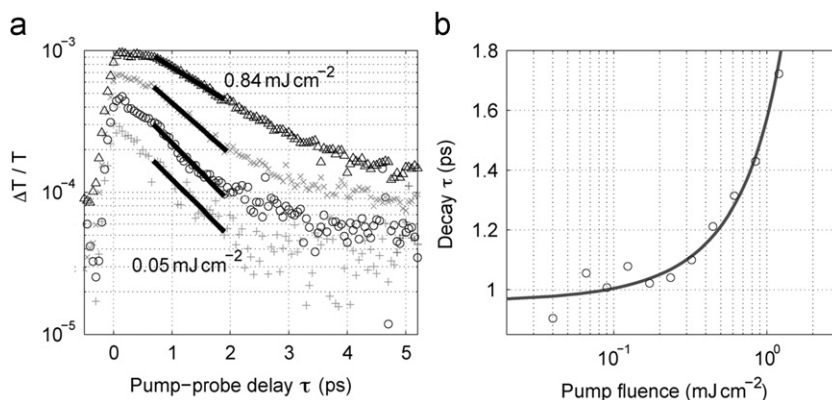


Fig. 9.5. (a) The photocarrier lifetime can be seen to increase with increasing fluence ( $0.05\text{--}0.84 \text{ mJ cm}^{-2}$ ). While the lifetime is non-monoexponential, a representative exponential decay can be fitted to a small section of the decay curve (shown as solid lines). (b) The extracted monoexponential carrier lifetime is shown as a function of incident fluence. The solid line is a numerical fit to a rate-equation model, as described in the text. Part b is reproduced with permission from [87].

to atmospheric oxygen. Radial heterojunction nanowires prepared via the techniques described in Section 7.2 are a model system for investigating the influence of surface trap density upon carrier dynamics.

Nanowires were grown with a GaAs core (40–60 nm diameter, 6–8  $\mu\text{m}$  length) which was overcoated with an AlGaAs shell ( $\sim 30$  nm) to encapsulate the surface. In addition, a skin layer of  $\sim 5$  nm of GaAs was deposited to prevent oxidation of the AlGaAs layer; however, this layer was not observed to play a part in the carrier dynamics of the nanowires. These GaAs core–AlGaAs shell–GaAs skin nanowires are known as core–shell–skin (CSS) nanowires and their growth details were given in Section 7.2. Fig. 9.6 shows clear improvement in carrier lifetime due to overcoating the nanowires, with a large increase in high-fluence carrier lifetime ( $4 \times$ ) [95]. The trapping process was separated into two parts: a saturable surface trap density, and a nanowire-specific non-saturable contribution. This permitted the modelling of the carrier lifetime using a coupled rate-equation model, which revealed an 82% reduction in surface trap density upon overcoating, which is similar to that achieved via sulphur surface passivation.

### 9.3. The influence of crystallographic defects

In addition to overcoating, we have recently investigated the influence of crystallographic twin defects by comparing nanowires grown via one-temperature or two-temperature process (as described in Section 5.2 and similar to those described in Section 8.5). By utilising the Drude–plasmon model (discussed in Section 9.1), and calculating the carrier mobility from the scattering rate, the impact of differing nanowire density on the substrate surface may be avoided. Fig. 9.7 shows the terahertz spectral conductivity at  $\sim 2$  ps after excitation for two sets of core–shell–skin nanowire samples: in one sample the GaAs cores were grown at  $450^\circ\text{C}$  via a one-temperature process (1T-CSS), and in the other sample nearly defect-free GaAs cores were grown at  $375^\circ\text{C}$  via the two-temperature technique (2T-CSS) (see Section 5.2 for core growth details) [95]. As can be seen, the improved growth

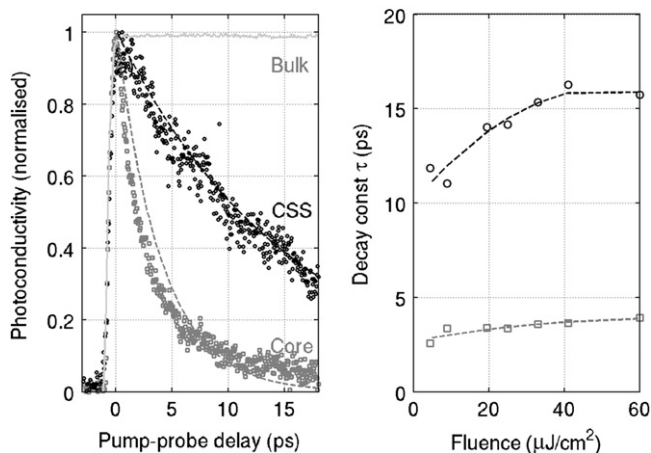


Fig. 9.6. The effect of heterojunction overcoating is demonstrated for AlGaAs coated GaAs nanowires. (Left) The photoconductivity transient is shown for bulk GaAs, core-only GaAs nanowires, and core–shell–skin (CSS) nanowires. (Right) The fluence-dependent carrier lifetime is shown for the CSS (circles) and core-only (squares) nanowires. Reproduced with permission from [95].

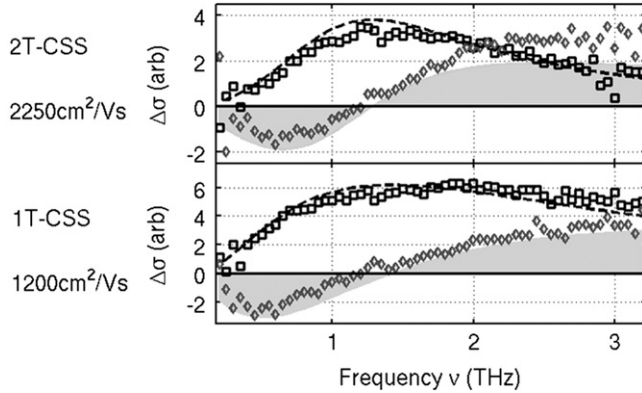


Fig. 9.7. The photoinduced conductivity spectrum of core–shell–skin nanowires is shown (at 2 ps after excitation with  $\sim 250 \mu\text{J cm}^{-2}$  per pulse). The upper pane shows the result for nanowires grown via a two-temperature process, revealing a large carrier mobility, whilst the lower pane shows the results for the one-temperature growth. Reproduced with permission from [95].

technique leads to an almost doubling in carrier mobility from 1200 to  $2250 \text{ cm}^2 \text{ V}^{-1} \text{ s}^{-1}$  which, in combination with other improvements to the growth technique represent a significant step towards exceptionally high optoelectronic quality nanostructures.

#### 9.4. Summary

In analysing an ensemble of GaAs nanowires using TCS we have established that electrons in nanowires propagate and interact with high-frequency electric fields in two ways. First, conductivity spectra reveal that a proportion of electrons behave in much the same way as electrons do in a bulk semiconductor, that is they undergo Drude transport. We assert that this contribution comes from nanowires with axes aligned in the direction of the applied electric field. Second, a non-Drude contribution to the conductivity spectrum comes from localised surface plasmon modes. These modes are coherent oscillations of the electron–hole plasma, which are modified from the bulk plasma frequency of the material by an interaction with the plasma/dielectric surface interface. We have assigned these modes to nanowires with axes perpendicular to the applied electric field.

Finally we have shown that photogenerated electrons in GaAs nanowires have both a remarkably high mobility and a very short lifetime. In addition, these parameters have been shown to be tunable via the initial growth conditions, allowing tailoring of the electronic behaviour of the nanowire for either fast switching or longer lifetime. Thus GaAs nanowires are ideal materials for applications in high-speed electronics. The detailed understanding of the transport of electrons in nanowires under the influence of high-frequency ( $\sim \text{THz}$ ) electric fields will be important for the design of future high-speed electronic devices from nanowires.

## 10. Conclusion

We have presented an Au-assisted MOCVD process to create high quality III–V nanowires and nanowire heterostructures in a flexible, tightly controlled and scalable manner. A number

of characterisation techniques have been presented, including electron microscopy, PL and TCS. Each of these techniques complements the others, and provides crucial information about the bandgap, carrier transport and optical properties of the nanowires. For instance, the presence of ZB/WZ polytypism within nanowire samples is determined by TEM, and then PL measurements reveal its major effect on nanowire optical properties. Nanowire properties can be carefully tuned during growth. For instance, we can grow bare GaAs nanowires with high mobility and very short carrier lifetime, which makes them ideal for high-speed electronics. On the other hand, when grown to be twin-free and clad in an AlGaAs shell, GaAs nanowires have a significantly enhanced lifetime, which makes them suitable for optical devices such as solar cells and photodetectors. These advances will enable a wide range of high performance nanowire-based quantum electronic and optoelectronic devices.

### **Acknowledgements**

We wish to thank our collaborators at the Australian National University (Jennifer Wong-Leung, Jung Hyun Kang, Suriati Paiman and Timothy Burgess), the University of Queensland (Mohanchand Paladugu, Xin Zhang, Yanan Guo), the University of Cincinnati (Thang Ba Hoang, Lyuba Titova, Melodie Fickenscher, Saranga Perera, Mohammad Montazeri) and the University of Oxford (Laura Herz). We thank the Australian Research Council, the National Science Foundation (Grants ECCS-0701703 and DMR-0806700), the Korean Science and Engineering Foundation (Grant F01-2007-000-10087-0) and the Engineering and Physical Sciences Research Council for financial support. The Australian National Fabrication Facility established under the Australian Government's National Collaborative Research Infrastructure Strategy, is gratefully acknowledged for providing access to the facilities used in this research.

### **References**

- [1] F. Patolsky, G. Zheng, O. Hayden, M. Lakadamyali, X. Zhuang, C.M. Lieber, *Proc. Natl. Acad. Sci. USA* 101 (2004) 14017–14022.
- [2] J.-I. Hahm, C.M. Lieber, *Nano Lett.* 4 (2004) 51–54.
- [3] D.J. Sirbulu, A. Tao, M. Law, R. Fan, P. Yang, *Adv. Mater.* 19 (2007) 61–66.
- [4] E.D. Minot, F. Kelkensberg, M. van Kouwen, J.A. van Dam, L.P. Kouwenhoven, V. Zwiller, M.T. Borgstrom, O. Wunnicke, M.A. Verheijen, E.P.A.M. Bakkers, *Nano Lett.* 7 (2007) 367–371.
- [5] Y. Huang, X. Duan, Charles M. Lieber, *Small* 1 (2005) 142–147.
- [6] F. Qian, S. Gradecak, Y. Li, C.-Y. Wen, C.M. Lieber, *Nano Lett.* 5 (2005) 2287–2291.
- [7] Y. Dong, B. Tian, T.J. Kempa, C.M. Lieber, *Nano Lett.* 9 (2009) 2183–2187.
- [8] B. Tian, X. Zheng, T.J. Kempa, Y. Fang, N. Yu, G. Yu, J. Huang, C.M. Lieber, *Nature* 449 (2007) 885–889.
- [9] J.A. Czuban, D.A. Thompson, R.R. LaPierre, *Nano Lett.* 9 (2009) 148–154.
- [10] Y. Xia, P. Yang, Y. Sun, Y. Wu, B. Mayers, B. Gates, Y. Yin, F. Kim, H. Yan, *Adv. Mater.* 15 (2003) 353–389.
- [11] R.S. Wagner, W.C. Ellis, *Appl. Phys. Lett.* 4 (1964) 89–90.
- [12] P.D. Markowitz, M.P. Zach, P.C. Gibbons, R.M. Penner, W.E. Buhro, *J. Am. Chem. Soc.* 123 (2001) 4502–4511.
- [13] M.A. Verheijen, G. Immink, T. de Smet, M.T. Borgström, E.P.A.M. Bakkers, *J. Am. Chem. Soc.* 128 (2006) 1353–1359.
- [14] K. Hiruma, M. Yazawa, K. Haraguchi, K. Ogawa, T. Katsuyama, M. Koguchi, H. Kakibayashi, *J. Appl. Phys.* 74 (1993) 3162–3171.
- [15] K.A. Dick, K. Deppert, T. Mårtensson, B. Mandl, L. Samuelson, W. Seifert, *Nano Lett.* 5 (2005) 761–764.
- [16] X. Duan, J. Wang, C.M. Lieber, *Appl. Phys. Lett.* 76 (2000) 1116–1118.



- [17] J.C. Harmand, M. Tchernycheva, G. Patriarche, L. Travers, F. Glas, G. Cirlin, *J. Cryst. Growth* 301–302 (2007) 853–856.
- [18] A.I. Persson, B.J. Ohlsson, S. Jeppesen, L. Samuelson, *J. Cryst. Growth* 272 (2004) 167–174.
- [19] K. Hiruma, H. Murakoshi, M. Yazawa, T. Katsuyama, *J. Cryst. Growth* 163 (1996) 226–231.
- [20] W. Seifert, M. Borgström, K. Deppert, K.A. Dick, J. Johansson, M.W. Larsson, T. Mårtensson, N. Sköld, C.P.T. Svensson, B.A. Wacaser, L.R. Wallenberg, L. Samuelson, *J. Cryst. Growth* 272 (2004) 211–220.
- [21] G.B. Stringfellow, *Organometallic Vapor-Phase Epitaxy: Theory and Practice*, Academic Press, San Diego, 1999.
- [22] K.A. Dick, *Prog. Cryst. Growth Charact. Mater.* 54 (2008) 138–173.
- [23] S.E.R. Hiscocks, W. Hume-Rothery, *Proc. R. Soc. London A* 282 (1964) 318–330.
- [24] J. Murray, H. Okamoto, T. Massalski, *J. Phase Equilibria* 8 (1987) 20–30.
- [25] H. Okamoto, *J. Phase Equilibria* 25 (2004) 197–198.
- [26] R. Elliott, F. Shunk, *J. Phase Equilibria* 2 (1981) 356–358.
- [27] H. Okamoto, T. Massalski, *J. Phase Equilibria* 5 (1984) 166–171.
- [28] H. Okamoto, T. Massalski, *J. Phase Equilibria* 5 (1984) 490–491.
- [29] H. Okamoto, T. Massalski, *J. Phase Equilibria* 5 (1984) 56–59.
- [30] C.T. Tsai, R.S. Williams, *J. Mater. Res.* 1 (1986) 820–826.
- [31] C.T. Tsai, R.S. Williams, *J. Mater. Res.* 1 (1986) 352–360.
- [32] C. Chatillon, F. Hodaj, A. Pisch, *J. Cryst. Growth* 311 (2009) 3598–3608.
- [33] K.A. Dick, K. Deppert, L.S. Karlsson, L.R. Wallenberg, L. Samuelson, W. Seifert, *Adv. Funct. Mater.* 15 (2005) 1603–1610.
- [34] M. Tchernycheva, J.C. Harmand, G. Patriarche, L. Travers, G.E. Cirlin, *Nanotechnology* 17 (2006) 4025.
- [35] M. Tchernycheva, L. Travers, G. Patriarche, F. Glas, J.-C. Harmand, G.E. Cirlin, V.G. Dubrovskii, *J. Appl. Phys.* 102 (2007) 094313.
- [36] A.I. Persson, M.W. Larsson, S. Stenström, B.J. Ohlsson, L. Samuelson, L.R. Wallenberg, *Nat. Mater.* 3 (2004) 677–681.
- [37] J.C. Harmand, G. Patriarche, N. Pere-Laperne, M.-N. Merat-Combes, L. Travers, F. Glas, *Appl. Phys. Lett.* 87 (2005) 203101.
- [38] G.A. Bootsma, H.J. Gassen, *J. Cryst. Growth* 10 (1971) 223–234.
- [39] S. Kodambaka, J. Tersoff, M.C. Reuter, F.M. Ross, *Science* 316 (2007) 729–732.
- [40] P. Cheyssac, M. Sacilotti, G. Patriarche, *J. Appl. Phys.* 100 (2006) 044315.
- [41] B.A. Wacaser, K.A. Dick, J. Johansson, M.T. Borgström, K. Deppert, L. Samuelson, *Adv. Mater.* 21 (2009) 153–165.
- [42] J. Johansson, C.P.T. Svensson, T. Mårtensson, L. Samuelson, W. Seifert, *J. Phys. Chem. B* 109 (2005) 13567–13571.
- [43] M.T. Borgström, G. Immink, B. Ketelaars, R.E. Algra, E.P.A.M. Bakkers, *Nat. Nano* 2 (2007) 541–544.
- [44] S.A. Dayeh, E.T. Yu, D. Wang, *Nano Lett.* 9 (2009) 1967–1972.
- [45] K.A. Dick, K. Deppert, L. Samuelson, W. Seifert, *J. Cryst. Growth* 297 (2006) 326–333.
- [46] M. Mattila, T. Hakkarainen, M. Mulot, H. Lipsanen, *Nanotechnology* 17 (2006) 1580.
- [47] F. Glas, J.C. Harmand, G. Patriarche, *Phys. Rev. Lett.* 99 (2007) 146101.
- [48] J. Zou, M. Paladugu, H. Wang, G.J. Auchtung, Y. Guo, Y. Kim, Q. Gao, H.J. Joyce, H.H. Tan, *C. Jagadish, Small* 3 (2007) 389–393.
- [49] J. Johansson, L.S. Karlsson, C.P.T. Svensson, T. Mårtensson, B.A. Wacaser, K. Deppert, L. Samuelson, W. Seifert, *Nat. Mater.* 5 (2006) 574–580.
- [50] M.A. Verheijen, R.E. Algra, M.T. Borgstrom, G. Immink, E. Sourty, W.J.P. van Enkevort, E. Vlieg, E.P.A.M. Bakkers, *Nano Lett.* 7 (2007) 3051–3055.
- [51] H.J. Joyce, Q. Gao, H.H. Tan, C. Jagadish, Y. Kim, X. Zhang, Y. Guo, J. Zou, *Nano Lett.* 7 (2007) 921–926.
- [52] H.J. Joyce, Q. Gao, H.H. Tan, C. Jagadish, Y. Kim, M.A. Fickenscher, S. Perera, T.B. Hoang, L.M. Smith, H.E. Jackson, J.M. Yarrison-Rice, X. Zhang, J. Zou, *Adv. Funct. Mater.* 18 (2008) 3794–3800.
- [53] H.J. Joyce, Q. Gao, H.H. Tan, C. Jagadish, Y. Kim, M.A. Fickenscher, S. Perera, T.B. Hoang, L.M. Smith, H.E. Jackson, J.M. Yarrison-Rice, X. Zhang, J. Zou, *Nano Lett.* 9 (2009) 695–701.
- [54] J. Vesenka, S. Manne, R. Giberson, T. Marsh, E. Henderson, *Biophys. J.* 65 (1993) 992–997.
- [55] J.H. Woodruff, J.B. Ratchford, I.A. Goldthorpe, P.C. McIntyre, C.E.D. Chidsey, *Nano Lett.* 7 (2007) 1637–1642.
- [56] S. Perera, M.A. Fickenscher, H.E. Jackson, L.M. Smith, J.M. Yarrison-Rice, H.J. Joyce, Q. Gao, H.H. Tan, *C. Jagadish, X. Zhang, J. Zou, Appl. Phys. Lett.* 93 (2008) 053110.

- [57] S. Paiman, Q. Gao, H.H. Tan, C. Jagadish, K. Pemasiri, M. Montazeri, H.E. Jackson, L.M. Smith, J.M. Yarrison-rice, X. Zhang, J. Zou, *Nanotechnology* 20 (2009) 225606.
- [58] H.J. Joyce, J. Wong-Leung, Q. Gao, H.H. Tan, C. Jagadish, *Nano Lett.* 10 (2010) 908–915.
- [59] S.K. Lim, M.J. Tambe, M.M. Brewster, S. Gradecak, *Nano Lett.* 8 (2008) 1386–1392.
- [60] Y. Kim, H.J. Joyce, Q. Gao, H.H. Tan, C. Jagadish, M. Paladugu, J. Zou, A.A. Suvorova, *Nano Lett.* 6 (2006) 599–604.
- [61] Y.N. Guo, J. Zou, M. Paladugu, H. Wang, Q. Gao, H.H. Tan, C. Jagadish, *Appl. Phys. Lett.* 89 (2006) 231917.
- [62] E. Ertekin, P.A. Greaney, D.C. Chrzan, T.D. Sands, *J. Appl. Phys.* 97 (2005) 114325.
- [63] M. Paladugu, J. Zou, Y.-N. Guo, X. Zhang, H.J. Joyce, Q. Gao, H.H. Tan, C. Jagadish, Y. Kim, *J. Appl. Phys.* 105 (2009) 073503.
- [64] M. Paladugu, J. Zou, Y.-N. Guo, Graeme J. Auchterlonie, Hannah J. Joyce, Q. Gao, H.H. Tan, C. Jagadish, Y. Kim, *Small* 3 (2007) 1873–1877.
- [65] M. Paladugu, J. Zou, G.J. Auchterlonie, Y.N. Guo, Y. Kim, H.J. Joyce, Q. Gao, H.H. Tan, C. Jagadish, *Appl. Phys. Lett.* 91 (2007) 133115.
- [66] M. Paladugu, J. Zou, Y.-N. Guo, X. Zhang, Y. Kim, H.J. Joyce, Q. Gao, H.H. Tan, C. Jagadish, *Appl. Phys. Lett.* 93 (2008) 101911.
- [67] M. Paladugu, J. Zou, Y.-N. Guo, X. Zhang, Hannah J. Joyce, Q. Gao, H.H. Tan, C. Jagadish, Y. Kim, *Angew. Chem.* 121 (2009) 794–797.
- [68] M. Paladugu, J. Zou, Y. Guo, X. Zhang, H. Joyce, Q. Gao, H. Tan, C. Jagadish, Y. Kim, *Nanoscale Res. Lett.* 4 (2009) 846–849.
- [69] M. Paladugu, J. Zou, Y.-N. Guo, X. Zhang, H.J. Joyce, Q. Gao, H.H. Tan, C. Jagadish, Y. Kim, *Appl. Phys. Lett.* 93 (2008) 201908.
- [70] X. Zhang, J. Zou, M. Paladugu, Y. Guo, Y. Wang, Y. Kim, H.J. Joyce, Q. Gao, H.H. Tan, C. Jagadish, *Small* 5 (2009) 366–369.
- [71] M.S. Gudiksen, J. Wang, C.M. Lieber, *J. Phys. Chem. B* 106 (2002) 4036–4039.
- [72] G. Zhang, K. Tateno, H. Sanada, T. Tawara, H. Gotoh, H. Nakano, *Appl. Phys. Lett.* 95 (2009) 123104.
- [73] A. Mishra, L.V. Titova, T.B. Hoang, H.E. Jackson, L.M. Smith, J.M. Yarrison-Rice, Y. Kim, H.J. Joyce, Q. Gao, H.H. Tan, C. Jagadish, *Appl. Phys. Lett.* 91 (2007) 263104.
- [74] S. Reitzenstein, S. Munch, C. Hofmann, A. Forchel, S. Crankshaw, L.C. Chuang, M. Moewe, C. Chang-Hasnain, *Appl. Phys. Lett.* 91 (2007) 091103.
- [75] N. Akopian, G. Patriarche, L. Liu, J.-C. Harmand, V. Zwiller, *Nano Lett.* 10 (2010) 1198–1201.
- [76] M.T. Borgström, V. Zwiller, E. Muller, A. Imamoglu, *Nano Lett.* 5 (2005) 1439–1443.
- [77] M.H.M. van Weert, N. Akopian, U. Perinetti, M.P. van Kouwen, R.E. Algra, M.A. Verheijen, E.P.A.M. Bakkers, L.P. Kouwenhoven, V. Zwiller, *Nano Lett.* 9 (2009) 1989–1993.
- [78] L.V. Titova, T.B. Hoang, H.E. Jackson, L.M. Smith, J.M. Yarrison-Rice, J.L. Lensch, L.J. Lauhon, *Appl. Phys. Lett.* 89 (2006) 053119.
- [79] L.V. Titova, T.B. Hoang, H.E. Jackson, L.M. Smith, J.M. Yarrison-Rice, Y. Kim, H.J. Joyce, H.H. Tan, C. Jagadish, *Appl. Phys. Lett.* 89 (2006) 173126.
- [80] T.B. Hoang, L.V. Titova, J.M. Yarrison-Rice, H.E. Jackson, A.O. Govorov, Y. Kim, H.J. Joyce, H.H. Tan, C. Jagadish, L.M. Smith, *Nano Lett.* 7 (2007) 588–595.
- [81] L.M. Smith, H.E. Jackson, J.M. Yarrison-Rice, C. Jagadish, *Semicond. Sci. Technol.* 25 (2010) 024010.
- [82] G.D. Gilliland, *Mater. Sci. Eng. R: Rep.* 18 (1997) 99–399.
- [83] L.V. Titova, T.B. Hoang, J.M. Yarrison-Rice, H.E. Jackson, Y. Kim, H.J. Joyce, Q. Gao, H.H. Tan, C. Jagadish, X. Zhang, J. Zou, L.M. Smith, *Nano Lett.* 7 (2007) 3383–3387.
- [84] M. Montazeri, M. Fickenschner, L.M. Smith, H.E. Jackson, J. Yarrison-Rice, J.H. Kang, Q. Gao, H.H. Tan, C. Jagadish, Y. Guo, J. Zou, M.-E. Pistol, C.E. Pryor, *Nano Lett.* 10 (2010) 880–886.
- [85] H.-K. Nienhuys, V. Sundstrom, *Appl. Phys. Lett.* 87 (2005) 012101.
- [86] R.H.M. Groeneveld, D. Grischkowsky, *J. Opt. Soc. Am. B* 11 (1994) 2502–2507.
- [87] P. Parkinson, J. Lloyd-Hughes, Q. Gao, H.H. Tan, C. Jagadish, M.B. Johnston, L.M. Herz, *Nano Lett.* 7 (2007) 2162–2165.
- [88] J.M. Pitarke, V.M. Silkin, E.V. Chulkov, P.M. Echenique, *Rep. Prog. Phys.* 70 (2007) 1–87.
- [89] J. Lloyd-Hughes, S.K.E. Merchant, L. Fu, H.H. Tan, C. Jagadish, E. Castro-Camus, M.B. Johnston, *Appl. Phys. Lett.* 89 (2006) 232102.
- [90] E. Castro-Camus, L. Fu, J. Lloyd-Hughes, H.H. Tan, C. Jagadish, M.B. Johnston, *J. Appl. Phys.* 104 (2008) 053113.

- [91] J. Lloyd-Hughes, S.K.E. Merchant, L. Sirbu, I.M. Tiginyanu, M.B. Johnston, *Phys. Rev. B* 78 (2008) 085320.
- [92] S.K.E. Merchant, J. Lloyd-Hughes, L. Sirbu, I.M. Tiginyanu, P. Parkinson, L.M. Herz, M.B. Johnston, *Nanotechnology* 19 (2008) 395704.
- [93] P.U. Jepsen, W. Schairer, I.H. Libon, U. Lemmer, N.E. Hecker, M. Birkholz, K. Lips, M. Schall, *Appl. Phys. Lett.* 79 (2001) 1291–1293.
- [94] V.N. Bessolov, M.V. Lebedev, *Semiconductors* 32 (1998) 1141–1156.
- [95] P. Parkinson, H.J. Joyce, Q. Gao, H.H. Tan, X. Zhang, J. Zou, C. Jagadish, L.M. Herz, M.B. Johnston, *Nano Lett.* 9 (2009) 3349–3353.